Flow Lattice Model for the Simulation of Chemistry Dependent Transport Phenomena in Cementitious Materials

Hao Yin* Antonio Cibelli† Susan-Alexis Brown* Lifu Yang‡ Lei Shen§
Mohammed Alnaggar¶ Gianluca Cusatis* Giovanni Di Luzio‖

February 21, 2023

Abstract

This study presents the formulation and validation of a three-dimensional (3D) Flow Lattice Model (FLM) with application to the Hygro-Thermo-Chemical (HTC) model for analysis of moisture transport and heat transfer in cementitious materials. The FLM is a discrete transport model formulated in association with meso-mechanical models, such as the Lattice Discrete Particle Model (LDPM). This enables the simulation of transport phenomena at the length scale at which the material exhibits intrinsic heterogeneity. The HTC theoretical formulation is based on mass and energy conservation laws, written using humidity and temperature as primary variables, and taking into account explicitly various chemical reactions, e.g. cement hydration and silica fume reaction, as internal variables. In this work, the HTC formulation was extended to include the effect of temperature on the sorption isotherm. The FLM solutions were compared with those of a continuum finite element implementation of the HTC model and experimental data available from the literature; the overall agreement demonstrates the reliability of the proposed approach in reproducing phenomena such as cement hydration, self-desiccation, temperature-dependent moisture drying, etc.

*Northwestern University, Department of Civil and Environmental Engineering, Evanston, Illinois, 60208, United States
†Politecnico di Milano, Department of Civil and Environmental Engineering, Milan, 20121, Italy
‡Hunan University, College of Civil Engineering, Changsha, 410082, China
§Hohai University, College of Water Conservancy and Hydropower Engineering, Nanjing, 210098, China
¶Oak Ridge National Laboratory, Oak Ridge, Tennessee, 37830, United States
‖Corresponding author: giovanni.diluzio@polimi.it

Key words

Discrete modeling, Moisture transport, Heat transfer, Cement hydration, Dual lattice

1 Introduction

The use of concrete as a building material is fundamental to the contemporary construction industry. Its historical prevalence combined with present-day ease of production, low labor cost, and versatile engineered properties has promoted concrete as an invaluable construction material. However, the construction industry, and in particular concrete production, is responsible for up to 10% of total CO_2 emissions per year. Cement clinker alone generates 0.9 tons of CO_2 per ton of material [1]. Reducing the resulting environmental effects is critical to safeguarding the future of construction. One factor which will lessen the impact of any material is improving the durability of the structure. Extending the service life time of concrete structures will minimize the need for new material production, and thus not only bring economic benefits but also reduce carbon emissions.

The durability of concrete structures is a function of a complex coupling between multi-physical phenomena, including the chemical aging process of the material, ingress of various deteriorating agents, and mechanical damage due to loads [2]. While design codes typically consider the suitability of the structures to sustain predicted loads at the time of construction, the long-term behavior of the structure may not be appropriately predicted, resulting in additional material and economic costs, and often compounding the initial carbon emissions. It is, therefore, necessary to adopt design principles which take into account the many facets which influence material durability to produce a structure with the optimal lifespan and thus minimize environmental impacts.

One of the primary causes of the deterioration of reinforced concrete is corrosion of the reinforcing steel, which can reduce tensile capacity and lead to spalling of the concrete cover [3]. This consequently shortens the service life of structures and increases maintenance costs. These effects are mitigated through the use of high-performance concrete (HPC) mixtures. Developed in the early 90's, HPC is characterized by low permeability and thus reduced risk of corrosion. Unfortunately, structures made from HPC are typically more vulnerable to cracking, especially at very early ages. The benefits of low permeability are completely lost when cracking initiates, as the cracks provide direct paths for corrosive agents to reach the reinforcing steel.

The cause of this early-age cracking in HPC is primarily attributed to resistance to volume changes

resulting from: (1) thermal expansion due to heat released by exothermic chemical reactions (cement hydration and pozzolanic reactions); (2) shrinkage due to water loss through exposed concrete surfaces (drying shrinkage); and (3) shrinkage due to water consumption during cement hydration and other chemical reactions (autogenous shrinkage). For normal strength concrete exposed to the environment, drying shrinkage dominates, but in the case of exposed HPC, in which autogenous and drying shrinkages combine, resulting in larger overall shrinkage [4].

As mentioned, these phenomena occur at early age, when the concrete strength and stiffness are still under rapid development and are directly influenced by curing conditions, such as temperature and relative humidity. The resulting overall shrinkage cannot, therefore, be easily predicted solely from the mix design. Thus, a reliable and predictive analysis of the concrete structure durability requires the formulation of a consistent theoretical and computational framework that includes all of the various phenomena characterizing the aging and evolution of concrete transport properties from early age. Therefore the characterization of moisture content, temperature evolution and reaction of cementitious materials are fundamental in this context.

In the literature, there are many experimental, theoretical, and computational studies on the behavior of concrete at early age. Studies on the analysis of self-desiccation include [5, 6, 7, 8], or both self-desiccation and drying such as [9, 10]. Many of the numerical models in the literature describe the cement hydration processes in conjunction with hygro-thermal and mechanical considerations. Among them, it is worth noting the dispersion model of [11] and the work of [12] with simple formulations for hydration based on spatial considerations, as well as the models of [13] and [14] that describe cement hydration based on the reaction kinetics and allow the evaluation of strength in time. In addition, [15] proposed a simple model that can take into account the effect of temperature on strength evolution, [16] developed a mesoscopic model for temperature and hydration degree in early-age concrete, and [17] proposed a simplified model to predict the internal relative humidity in early-age concrete under different curing humidity conditions.

More complex models allow the description of hydration, heat diffusion, moisture transport, chemical shrinkage, and self-desiccation [18, 19, 20, 21, 22, 23]. Among them, the Hygro-Thermo-Chemical (HTC) model proposed by [24, 25] formulates the evolution of cement hydration and of pore relative humidity in concrete, based on moisture transport and heat transfer governing equations. The model uses phenomenological evolution laws to describe the reaction degrees for cement and silica fume, and the associated changes in evaporable and chemically bound waters, along with adsorption/desorption isotherms

and permeability of concrete. The capability of the HTC model has been demonstrated through extensive numerical studies by many authors [25, 26, 27, 28, 29, 30, 31, 32]. Recently, a multiscale approach, entitled the ONIX model, has been proposed in [33], where all the parameters governing the HTC constitutive relations are identified by using the output of micro-scale numerical simulations carried out by the CEMHYD3D model [34, 35].

The influence of cracking on the mass transport, which governs many engineering applications of construction materials, is still a challenge from the numerical modeling point of view and different approaches are reported in the literature. Some models are based on continuum mechanics [36, 31], while others combine continuum mechanics with discrete representation of cracks [37, 38, 39, 40]. Conversely, discrete approaches, such as discrete element method, lattice and network models, have been formulated to simulate cracking, mass transport and their coupling, as in [41, 42, 43, 44, 45, 46, 47, 48, 49]. It is worth mentioning one network approach based on the Delaunay tessellation of a random set of points [48, 49]. In this approach, the physical transport processes have been first simulated by a multi-dimensional network of 1D elements placed on the Delaunay edges, and the element properties are determined by the corresponding Voronoi tessellation [48]. In a later study, the transport elements were placed on the Voronoi edges (i.e. a dual network), maintaining the structural elements on the Delaunay edges [49]. With this approach, the crack effects on diffusion processes are more physically reproduced, as the transport elements aligned with the crack directions. However, in this method, as well as in most other models in the literature, the discrete feature of the model is not related to the actual heterogeneity of the material. This feature is critical when transport processes are considered in cementitious heterogeneous materials, as demonstrated for chloride transport in concrete, particularly in non-saturated conditions, see [50].

The Lattice Discrete Particle Model (LDPM), originally proposed by Cusatis et al. [51, 52], is a discrete model simulating concrete material heterogeneity at the mesoscale (coarse aggregate) and has proven its capability in accurately simulating many mechanical behaviors, especially the mesoscale failure behaviors of concrete materials [53, 54, 55, 56, 57, 58, 59, 60]. Some explorations of the capability of the LDPM in solving multiphysics problems have also been performed recently [61, 62, 63, 64, 50, 65]. The Multiphysics Lattice Discrete Particle Model (M-LDPM) is formulated and fully integrated with the existing LDPM to extend the capability of LDPM for solving multiphysics problems, such as moisture diffusion, heat transfer, chloride diffusion, and crack healing within the LDPM framework [61, 62, 63, 64, 50, 66].

The objective of this study is to present the first step towards the formulation of the 3D Flow Lattice

Model (FLM) with application to the HTC model. The FLM approach forfeits the continuum assumption by way of discrete modeling at the mesoscale from the LDPM geometry. This means that FLM can more accurately consider damage and its localization in cracks by discontinuities between adjacent cells and it is able to reproduce critical features of material heterogeneity being 3D flow network based on the LDPM geometry. This work, which focuses only on the first point, presents the new formulation of the 3D FLM which represents an important development in the field of concrete construction in which reliable predictive numerical model of the chemo-transport phenomena are fundamental to design durable and, therefore, sustainable structures and infrastructures. Also, the quality of the FLM results are verified by comparing the FLM solutions with the finite element solutions since both of them must converge to the analytical solution when the size of the discretizing mesh decreases and same constitutive laws with same parameters are employed.

In the following paper, the balance equations of moisture transport and heat transfer are derived in the discrete context, and the theoretical HTC formulation is outlined. Then, the numerical implementation is presented and validated using a selection of experimental data available in the literature. For the first time, the effect of the temperature on the moisture diffusion is also verified. The FLM full coupling with LDPM, i.e. effects of damage, micro-cracks, and cracks, as well as the updates and improvements of the HTC formulation at the mesoscale are behind the scope of the manuscript and are left for future work.

2 The Flow Lattice model

2.1 The Lattice Discrete Particle Model (LDPM) tessellation and the Flow Lattice Model (FLM) network

A pair of topologically dual and coupled lattice systems are involved in LDPM. One is referred to as the LDPM cell system, which provides a geometrical characterization for mechanical behaviors of concrete. The other is referred to as the *Flow Lattice Model* (FLM) system - the key focus of this work - which provides the geometrical characterization of the flow (diffusive) behaviors of concrete.

The geometric representations of the discrete models, including LDPM and FLM, are crucially important for representing the model behaviors with high fidelity. To capture the granular nature of the concrete internal mesostructure, LDPM discretizes the model domain with randomly packed polyhedral cells, which represent the coarse aggregate particles embedded in a cementitious fine mortar (hereinafter referred as LDPM tessellation). The cell size corresponds to the length scale at which the significant

material heterogeneities (coarse aggregates fields) are observed. The construction of the dual lattice systems is briefly summarized hereinafter, and the details of the tessellation can be found in [51]. (i) Idealized spherical particles that approximate the aggregate particles of concrete are randomly packed in the model domain without overlapping. The particle size distribution curve follows a Fuller sieve curve to reproduce realistic concrete mesostructures. Over the model boundaries, nodes (equivalent to zero-radius aggregates) are randomly placed. A typical aggregate distribution is shown in Fig. 1a. (ii) Given the particle centers, a constrained Delaunay tetrahedralization [51] is performed to divide the domain volume with a mesh of tetrahedra (LDPM tets, as shown in Fig. 1b). In each LDPM tet, 12 LDPM facets are constructed by sequentially locating edge points E_{ij}, face points F_k, and a tet point N and forming small triangular facets "$NE_{ij}F_k$". (explain here face/edge/tet point) The construction of LDPM facets can be illustrated as follows (see also [51]): edge-points are defined at midways of the edges belonging to the associated particles (E_{12} for P_1 and P_2 in Fig. 1b). Regarding the face-points, on each face of the tetrahedron, the midway point (for example, F_4 for face 4) located on the straight lines connecting each face vertex to the edge-point located on the edge opposite to the particle under consideration are identified as face points. Regarding the edge-points, these points locate at midway of the line counterpart not belonging to the associated particles. In Fig. 1b, the point F_4 associated with vertex P_3 and edge-point E_{12} is shown. The tet-point is defined as the centroid identified on the straight lines connecting each vertex of the tetrahedron with the face-point on the face opposite to the vertex under consideration and located at midway of the line counterpart not belonging to the associated particle. The tet-point N associated with vertex P_4 is shown in the Fig. 1b. Finally, a LDPM tet with its all 12 LDPM facets is shown in Fig. 1c.

(iii) The model domain is then subdivided through these LDPM facets into a system of polyhedral cells. The surfaces of the polyhedral cells (consisting of LDPM facets, as shown in Fig. 1d) define the potential failure locations. The prerequisite of this statement is that, the LDPM mesoscale geometry in which polyhedral cells containing each particle are assumed rigid and those rigid discrete cells are in contact through the facets in which stress and strain are defined and where the deformation takes place. Therefore, the surface of the polyhedral cells (LDPM facets) represents the potential failure location, i.e., where deformation and cracking can happen (the cell is rigid and can't deform). The LDPM cells and the tessellated model domain are shown in Fig. 1e and f, respectively.

(iv) With the tessellated domain, a flow network can be formed by connecting the tet points belonging to each pair of two adjacent LDPM tetrahedra (Fig. 1g) with 1D line elements (e.g., N_1N_2 line segment

in Fig. 1h), the resulting network is shown in Fig. 1i.

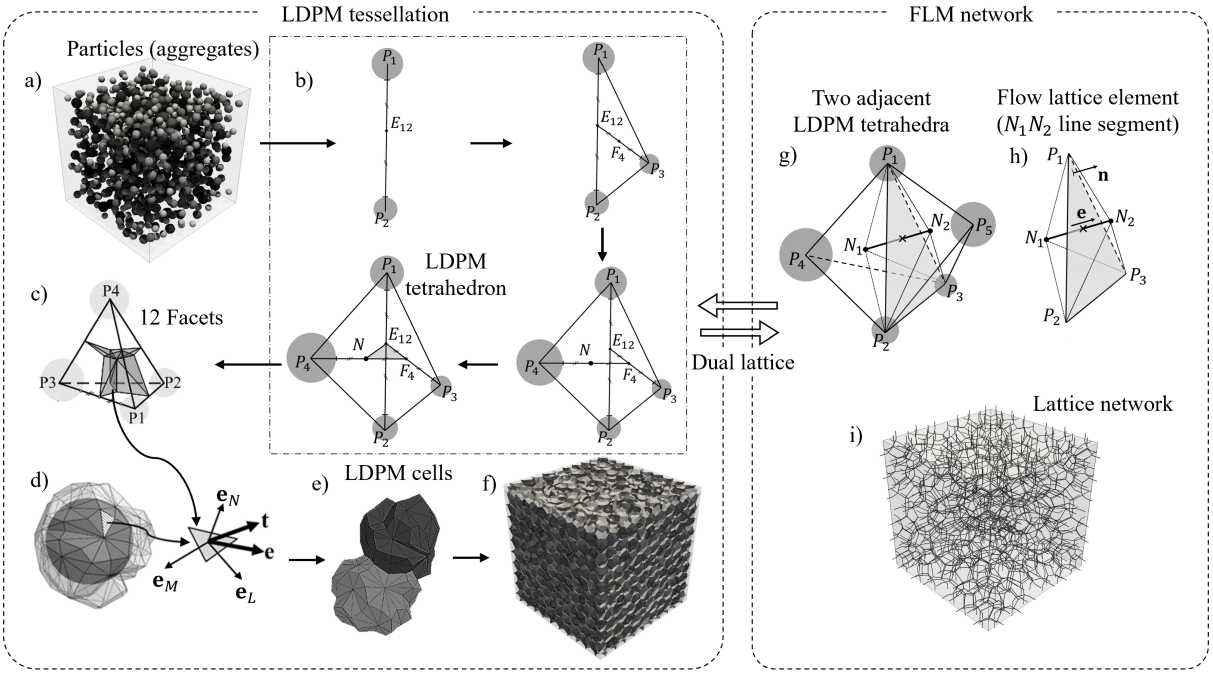

Figure 1: Lattice Discrete Particle Model (LDPM) tessellation and *Flow Lattice Model* network: a) idealized particles (aggregates) in the specimen, b) the construction of the LDPM tetrahedron (tet) from the creation of edge points E_{ij}, to that of face points F_k and tet points N, and finally to the formation of triangular facets "$NE_{ij}F_k$", c) LDPM tet element with 12 facets, d) a particle surrounded by associated LDPM facets, e) two adjacent LDPM cells, f) a typical LDPM tessellated specimen, g) two adjacent LDPM tetrahedra and their tet points N_1, N_2, h) the associated *Flow Lattice Element* N_1N_2, and i) the flow lattice network

The basic unit of the FLM network is called a *Flow Lattice Element* (FLE), where each FLE can be seen as a small conduit across the boundary of two adjacent LDPM tets (Fig. 2a). The properties of each FLE are characterized by the geometries of the associated tetrahedra, and potentially by the relative motions (e.g. crack openings) of the pairs of tetrahedra. The domain volume (V) of a FLE consists of two pyramids, referred as "side N_1" (V_1) and "side N_2" (V_2). The segment length of FLE, l, can be decomposed into two segments at the intersection of line segment with the tetrahedron surface $P_1P_2P_3$ (Fig. 2b). The segment lengths l_1 and l_2 associated with side N_1 and side N_2 can be defined by the length proportionality coefficients $0 \leq g_1 \leq 1$ and $0 \leq g_2 \leq 1$, which satisfy the relations $l_i = g_i l$ $(i = 1, 2)$. As shown in Fig. 2b, $\mathbf{n}$ is the unit normal vector of the surface $P_1P_2P_3$, and $\mathbf{e}$ is the direction vector of FLE from N_1 to N_2. The projected area of triangular cross-section $P_1P_2P_3$ (A_0) in the $\mathbf{e}$ direction is defined as $A = |\mathbf{n} \cdot \mathbf{e}|A_0$. One can write $V = V_1 + V_2 = Al/3$, generally, the normal vector $\mathbf{n}$ is not necessarily parallel to direction vector $\mathbf{e}$.

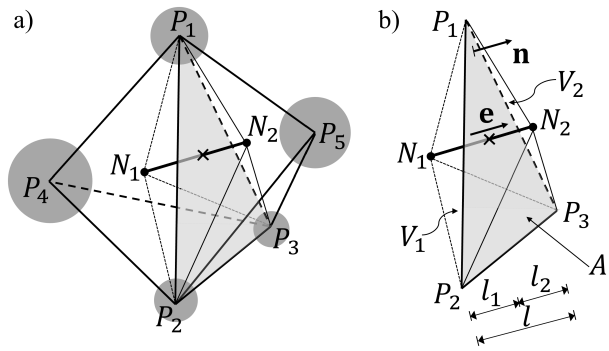

Figure 2: Diagrams of the *Flow Lattice Element* (FLE): a) FLE generation from the dual LDPM tetrahedra b) FLE geometry

Three types of FLE exist: regular (or type 1) elements - all interior elements belong to this category, as depicted in Fig. 3a; transitional layer (or type 2) elements, which corresponds to the elements having two nodes - one interior tet point and the other on the boundary of the whole model, as depicted in Fig. 3b; boundary layer (or type 3) elements, which shares the node on the boundary of a type 2 element, and then extends orthogonally to the outside of the model boundary. Different from type 1 and type 2, the boundary layer element consists of two triangular prisms with equal volumes $V_1 = V_2$ and equal segment lengths $l_1 = l_2$, as depicted in Fig. 3c. Type 3 elements are used to enforce the boundary conditions; details will be discussed in following sections. The formulation of FLEs is the same for all types of elements, but the term values are governed by the geometric properties of different element types.

2.2 Balance equations for moisture transport and heat transfer in the Flow Lattice Element (FLE)

For the transport problem of water mass and heat in concrete, the relative humidity h and temperature T are selected as the primary fields (a.k.a. the degrees of freedom in numerical analyses). The values at LDPM tet points N_1 and N_2, i.e., h_i, T_i $(i = 1, 2)$ represent the mass thermodynamic state in the control volume of the FLE.

The water mass and heat balance equations in a FLE control volume V consisting of V_1 and V_2, can be obtained from mass and enthalpy conservation laws, which read

$$V_1\dot{w} + Aj_h = 0 \qquad V_1\dot{U} + Aj_T + V_1 q_T = 0 \qquad V_2\dot{w} - Aj_h = 0 \qquad V_2\dot{U} - Aj_T + V_2 q_T = 0 \tag{1}$$

where the dot accents denote the time rates of variables, $w = w(h, T)$ and $U = U(h, T)$ stand for the

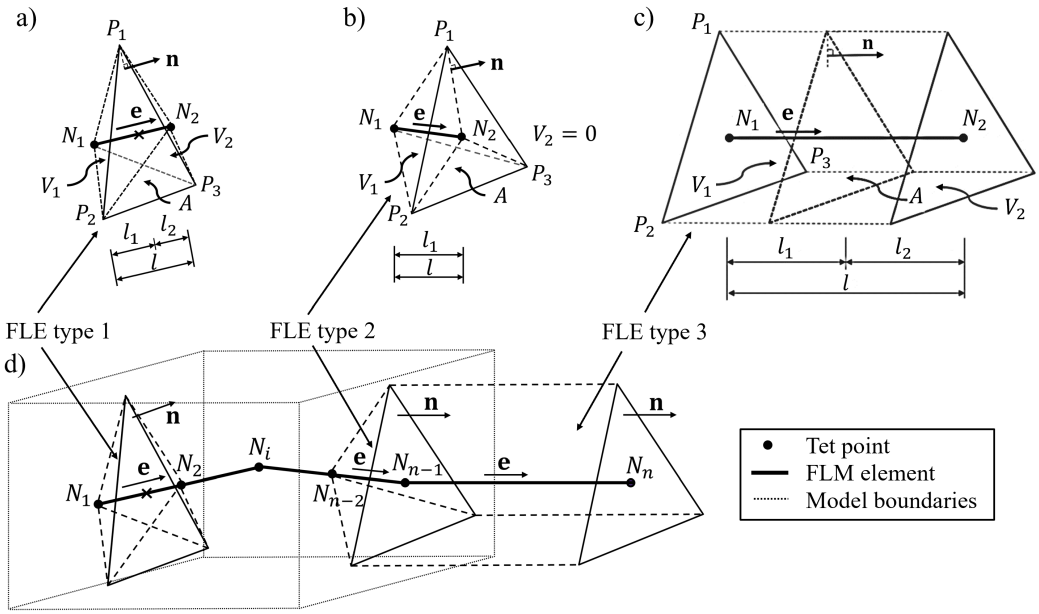

Figure 3: Illustrative diagrams of various *Flow Lattice Element* (FLE) types: a) regular (type 1) element, $V = V_1 + V_2$, $g_1 = l_1/l$, $g_2 = l_2/l$, $\mathbf{e} \nparallel \mathbf{n}$; b) transitional layer (type 2) element, $V = V_1$, $V_2 = 0$, $g_1 = 1$, $g_2 = 0$, $\mathbf{e} \nparallel \mathbf{n}$; (c) boundary layer (type 3) element, $V = V_1 + V_2$, $V_1 = V_2$, $g_1 = 1/2$, $g_2 = 1/2$, $\mathbf{e} \parallel \mathbf{n}$; d) FLEs in the model

total water mass content and internal energy per unit volume, j_h and j_T stand for the flux density of water mass and heat per unit time associated with the projected section area A, a positive flux is defined entering V_1 from V_2; q_T stands for the source term of thermal energy. The material volumes V_1, V_2, and their common projected section area A are considered to be constant in this study.

In concrete, water is present in multiple phases [67, 68, 69]: (a) capillary water, (b) water vapor, (c) adsorbed water, and (d) non-evaporable (chemically bound) water. Water that is chemically combined with other chemical compounds loses its mobility completely and cannot contribute to moisture transport. In the literature, chemically bound water is typically referred to as non-evaporable water, as it is retained even at temperatures not exceeding 105 °C. Generally, the transport mechanisms of each phase should be modeled independently through the formulation of separate diffusion equations, as each mechanism has its own driving force, e.g. capillary pressure for the capillary water, vapor pressure for the water vapor, etc.). However, the computational cost of such complex phenomena calls for a simplified analysis. First, it is possible to simplify the problem by postulating the existence of a local thermodynamic equilibrium ([69, 70, 18]). This assumption also holds approximately in the presence of chemical evolution of the system (aging) as the characteristic time scale of the water transport mechanisms is much smaller than those associated with concrete chemical reactions.

The total water content w, can be expressed as $w = w_e + w_n$, where w_e represents the evaporable water portion, which comprises capillary water, water vapor, and adsorbed water, and w_n represents the non-evaporable (chemically bound) water [71, 72]. The relation between the evaporable water and relative humidity h, is the so called *sorption isotherm* which is here assumed also to be function of temperature T, the degree of hydration, α_c, and the degree of silica-fume reaction, α_s, i.e. $w_e = w_e(h, T, \alpha_c, \alpha_s)$ (age-dependent *adsorption/desorption isotherm* [73]). The water content variation in time reads

$$\dot{w} = \dot{w}_e + \dot{w}_n = \frac{\partial w_e}{\partial h}\dot{h} + \frac{\partial w_e}{\partial T}\dot{T} + \frac{\partial w_e}{\partial \alpha_c}\dot{\alpha}_c + \frac{\partial w_e}{\partial \alpha_s}\dot{\alpha}_s + \dot{w}_n \tag{2}$$

where $\partial w_e/\partial h$ is the slope of the sorption isotherm (also called *moisture capacity*), $\partial w_e/\partial T$ represents the variation of the evaporable water with respect to the temperature variation, and the last three terms express the effect of concrete aging on the diffusion process; the first two terms account for the microstructural changes associated with the concrete chemical reactions and the last term accounts for the internal "consumption" of water involved in the chemical reactions, called *moisture sink*, explains the well-known *self-desiccation* phenomenon.

For the temperature range considered in this study (10–100 °C), no phase change is happening in concrete [74], hence the thermal energy variation in time reads $\dot{U} = \rho c_t \dot{T}$, where ρ is the mass density and c_t is the isobaric heat capacity (specific heat) of concrete, assumed as $c_t = 1100$ J/kg°C, which may be generally adopted for all concretes. The product ρc_t is the *thermal capacity.*

In this study, all moisture transport mechanisms are combined into a single phenomenological equation ([69, 75, 76]) and the overall moisture transport process under isothermal conditions is described through an equivalent Fick's law $j_h = -D_h(h, T)g_h$, where j_h is the flux density of water mass per unit time, g_h is the discrete estimation of relative humidity gradient, which read $g_h = \mathbf{e} \cdot \mathbf{n}(h_2 - h_1)/l$, the proportionality coefficient $D_h(h, T)$, called *moisture permeability*, is a nonlinear function of relative humidity h and temperature T [75]. The choice of relative humidity h as the state variable of the problem (in addition to the temperature T) is done here for convenience but other options can be equivalently adopted [70].

Heat conduction can be described in concrete by classical Fourier's law as $j_T = -\lambda g_T$, where j_T stands for the heat flux density per unit time, g_T stands for the discrete estimation of the temperature gradient, which reads $g_T = \mathbf{e} \cdot \mathbf{n}(T_2 - T_1)/l$. For temperatures below 100°C, the heat conductivity of concrete, λ, may be assumed constant and a value of $\lambda = 2.3$W/m°C [74, 77] will be used for the numerical simulations presented in the following sections.

The source term of thermal energy q_T, can be expressed as $q_T = \dot{Q}_c + \dot{Q}_s$, in which $\dot{Q}_c$ and $\dot{Q}_s$, represent

the rate of heat generation per unit volume due to cement hydration and silica fume (pozzolanic) reaction, respectively. They read

$$\dot{Q}_c = \dot{\alpha_c}\ c\ \tilde{Q}_c^{\infty} \qquad\qquad \dot{Q}_s = \dot{\alpha_s}\ s\ \tilde{Q}_s^{\infty} \tag{3}$$

where $\dot{\alpha_c}$ is the rate of the hydration degree, as discussed following, c is the cement mass content, $\dot{\alpha_s}$ is the rate of pozzolanic reaction degree, also discussed following, and s is the silica fume mass content. The latent heat of hydration reaction per unit of hydrated mass, $\tilde{Q}_c^{\infty}$, may be assumed constant for a given concrete as it depends only on the chemical composition of its cement [78, 13, 79, 15, 18]. It can be measured in calorimetric tests at complete hydration and typical values range from 400 kJ/kg to 550 kJ/kg depending upon cement composition [80]. The enthalpy of silica fume, $\tilde{Q}_s^{\infty}$, can be assumed constant and equal to 780 kJ/kg [81].

By substituting Eqs. 2, 3 and collecting all the other entries described above, one can expand the governing equations Eqs. 1 as

$$\begin{aligned}
V_1\left(\frac{\partial w_e}{\partial h}\dot{h} + \frac{\partial w_e}{\partial T}\dot{T} + \frac{\partial w_e}{\partial \alpha_c}\dot{\alpha_c} + \frac{\partial w_e}{\partial \alpha_s}\dot{\alpha_s} + \dot{w}_n\right) + AD_h\frac{h_2 - h_1}{l}\mathbf{e}\cdot\mathbf{n} = 0 \\
V_1\left(\rho c_t\dot{T} + \dot{\alpha_s}\ s\ \tilde{Q}_s^{\infty} + \dot{\alpha_c}\ c\ \tilde{Q}_c^{\infty}\right) + A\lambda\frac{T_2 - T_1}{l}\mathbf{e}\cdot\mathbf{n} = 0 \\
V_2\left(\frac{\partial w_e}{\partial h}\dot{h} + \frac{\partial w_e}{\partial T}\dot{T} + \frac{\partial w_e}{\partial \alpha_c}\dot{\alpha_c} + \frac{\partial w_e}{\partial \alpha_s}\dot{\alpha_s} + \dot{w}_n\right) - AD_h\frac{h_2 - h_1}{l}\mathbf{e}\cdot\mathbf{n} = 0 \\
V_2\left(\rho c_t\dot{T} + \dot{\alpha_s}\ s\ \tilde{Q}_s^{\infty} + \dot{\alpha_c}\ c\ \tilde{Q}_c^{\infty}\right) - A\lambda\frac{T_2 - T_1}{l}\mathbf{e}\cdot\mathbf{n} = 0
\end{aligned} \tag{4}$$

3 The Hygro-Thermo-Chemical (HTC) model

The HTC model [24, 25], simulating the moisture and temperature evolution in a cementitious material considering the simultaneous chemical reactions, i.e. hydration of cement and pozzolanic reactions, is here recalled.

3.1 Cement hydration

The cement hydration is the result of the reaction between the free water and the cement particles, which are primarily composed of calcium silicates (C_3S and C_2S) and calcium aluminates (C_3A and C_4AF). The products of the cement hydration are calcium silicates hydrates (CSH), calcium hydroxide (CH), ettringite (Aft), and monosulfate (Afm) [82]. Since the precise stoichiometry of the chemical reactions involved is not exactly known and their mutual interaction, as well as the influence of external

factors (such as temperature, relative humidity, etc.), are not completely understood [82, 74], many researchers [83, 84, 79, 15, 18] have studied cement hydration with reference to an overall hydration process without distinction among the hydration reactions of every single compound. The present model also adopts this approach.

Following the thermodynamics-based model proposed in [84, 85, 15], the hydration kinetics can be described by postulating the existence of a Gibb's free energy that is dependent on the external temperature T and the *hydration extent* χ_c. The hydration extent can be used to define a normalized measure of the hydration process, the *hydration degree*, as $\alpha_c = \chi_c/\overline{\chi}_c^{\infty}$, in which $\overline{\chi}_c^{\infty}$ is the theoretical asymptotic values of the hydration extent in ideal hygrometric conditions. Since the actual asymptotic value of hydration extent, χ_c^{∞}, is always smaller than the theoretical value, $\overline{\chi}_c^{\infty}$, the ratio between the actual and the theoretical asymptotic values is the asymptotic degree of hydration $\alpha_c^{\infty} = \chi_c^{\infty}/\overline{\chi}_c^{\infty}$, which has been shown to be always smaller than unit [80].

By assuming that the hydration extent is driven by the thermodynamic force conjugate to it, the so-called *chemical affinity*, and governed by an Arrhenius-type expression, the following evolution equation for the hydration degree can be written [84, 15].

$$\dot{\alpha}_c = A_c(\alpha_c)\ e^{-E_{ac}/RT} \qquad \text{with} \qquad A_c(\alpha_c) = A_{c1}\left(\frac{A_{c2}}{\alpha_c^{\infty}} + \alpha_c\right)(\alpha_c^{\infty} - \alpha_c)\ e^{-\eta_c \alpha_c/\alpha_c^{\infty}} \tag{5}$$

where $A_c(\alpha_c)$ is the so called *normalized chemical affinity*, E_{ac} is the hydration activation energy, R is universal gas constant, and η_c, A_{c1}, A_{c2} are material parameters. In the present study the value E_{ac}/R = 5000 K will be adopted in absence of specific measurements. The parameters η_c, A_{c1}, A_{c2} can be calibrated by simulating the temperature evolution during adiabatic tests, see [25].

Moreover, it is well known from experiments that if the relative humidity decreases below a certain value ($h \approx 75\%$), the hydration process slows down and may even stop [68, 86]. This phenomenon can be taken into account [18] by rewriting Eq. 5 as

$$\dot{\alpha}_c = A_c(\alpha_c)\ \beta_h(h)\ e^{-E_{ac}/RT} \qquad \text{with} \qquad \beta_h(h) = \left[1 + (a - ah)^b\right]^{-1} \tag{6}$$

The function $\beta_h(h)$ is an empirical function with the parameters a and b that may be calibrated through the analysis of experimental data but constant values of $a = 5.5$ and $b = 4$ are generally adopted [18, 25].

3.2 Pozzolanic reaction from silica-fume

Silica fume (SF) is often added in the concrete mixture in order to produce HPC [87, 88]. SF belongs to the category of highly pozzolanic materials and it consists of silica in noncrystalline form with a high specific surface and exhibiting high pozzolanic activity. The pozzolanic reactions occur between the silica-rich SF particles and the portlandite (CH) generating Calcium Silicate Hydrates (CSH) [89]. The exact stoichiometry of pozzolanic reaction between SF and CH is not exactly known, especially in relation to the water stoichiometry coefficient. As current literature presents dissonant results on this issue, it is assumed that no water is involved (consumed or released) in the SF pozzolanic reaction [90].

The effect of SF on moisture and heat diffusion phenomena is here modeled through the introduction of the degree of SF reaction, α_s, defined as the ratio between the amount of reacted SF and the total amount of SF. Since the kinetics of the pozzolanic reaction can be assumed to be a diffusion-controlled process [91, 92, 93], the theory adopted in the previous section to describe cement hydration can be exploited here to describe the evolution of SF reaction. Accordingly, one has

$$\dot{\alpha_s} = A_s(\alpha_s)\ e^{-E_{as}/RT} \qquad \text{with} \qquad A_s(\alpha_s) = A_{s1}\ \left(\frac{A_{s2}}{\alpha_s^\infty} + \alpha_s\right)(\alpha_s^\infty - \alpha_s)\ e^{-\eta_s \alpha_s/\alpha_s^\infty} \tag{7}$$

where A_s is the SF normalized affinity, E_{as} is the activation energy of SF reaction, and α_s^∞ is the asymptotic value of SF reaction degree. $E_{as}/R = 9700$ K can be generally assumed [80]. The material parameters A_{s1}, A_{s2} and η_s can be calibrated similarly to the parameters governing cement hydration [25].

When a sufficient amount of SF is available in concrete, all the CH produced by the cement hydration can be consumed by the pozzolanic reaction. For water-to-cement ration, w/c, of about 0.5 (normal concrete), about 16% silica fume is required to consume all the calcium hydroxide during the pozzolanic reaction [94]. For lower values of w/c, the required amount of silica fume to consume all the calcium hydroxide is reduced proportionally and the proportionality coefficient of 0.4 can be used as confirmed by experiments on carbonation shrinkage [94]. According to these observations, the asymptotic degree of SF reaction degree is expressed as

$$\alpha_s^\infty = SF^{eff} \qquad \text{if} \qquad \begin{cases} s/c < 0.16 & \text{and} \quad w/c > 0.4, \\ s/c < 0.4(w/c) & \text{and} \quad w/c \leq 0.4. \end{cases} \tag{8}$$

where s/c is the silica-to-cement ratio and SF^{eff} is the "efficiency" of silica fume, i.e. the mass ratio

between the SiO_2 mass content and the total mass of silica fume. Because only the SiO_2 participates in the pozzolanic reaction, the remaining portion of SF does not participate in any chemical reaction and has the role of an inert filler. Typically, SF_{eff} ranges from 0.85 to 0.92 [82]. If the amount of silica fume exceeds the minimum required amount of silica fume to consume all the calcium hydroxide, the asymptotic degree of SF reaction is less than SF^{eff}. Assuming a linear relationship between α_s^∞ and s/c, the asymptotic degree of SF reaction degree can be estimated as

$$\alpha_s^\infty = \begin{cases} \frac{SF^{eff}\ 0.16}{s/c} & \text{if } \ w/c > 0.4, \\ \frac{SF^{eff}\ 0.4(w/c)}{s/c} & \text{if } \ w/c \leq 0.4. \end{cases} \tag{9}$$

3.3 Asymptotic hydration degree

The asymptotic (ultimate) hydration degree, α_c^∞, is always less than one [80], as a unit value can be reached only in ideal conditions that in practice are never fulfilled during curing [68].

As proposed by Pantazopoulo and Mills [72], α_c^∞ may be calculated on the basis of a mass balance between water needed to ensure saturation conditions and total water content. This balance gives

$$\alpha_c^\infty = \frac{1.031\ w/c}{0.194 + w/c} \tag{10}$$

However, the presence of SF further reduces the ultimate achievable hydration degree because, due to the formation of additional CSH gel from the pozzolanic reaction, additional water is hindered in entering the gel pores and it becomes unavailable for the cement hydration reaction [80]. As proposed by Di Luzio and Cusatis [24], α_c^∞ can be expressed in the presence of SF as

$$\alpha_c^\infty = \frac{1.032 w/c - 0.279(s/c)\alpha_s^\infty}{0.194 + w/c} \tag{11}$$

where s is SF content, and α_s^∞ is the asymptotic SF reaction degree given by Eqs. 8 and 9. Note that the minus sign in Eq. 11 expresses the fact that in presence of SF the asymptotic degree of hydration is reduced because the SF pozzolanic reaction increases the specific surface of the CSH gel making unhydrated cement grain cores less accessible.

3.4 Non-evaporable and evaporable water

In the present model, the non-evaporable water is the amount of water that is chemically bound as a consequence of cement hydration and SF reaction, and is computed as

$$w_n(\alpha_c, \alpha_s) = \kappa_c \alpha_c c + \kappa_s \alpha_s s \tag{12}$$

where κ_c represents the mass ratio of non-evaporable water at full hydration and κ_s represents the mass ratio of SF content at full SF reaction.

The content of evaporable water is characterized through its relationship with relative humidity, the so-called "adsorption isotherm" if obtained with increasing relativity humidity, or "desorption isotherm" in the opposite case. The adsorption and desorption isotherms are typically not the same; a hysteresis is observed during adsorption/desorption cycles [95, 96]. This has been explained in [97] as a consequence of two related mechanisms: snap-through instabilities during the filling or emptying of non-uniform nanopores or nanoscale asperities, and the molecular coalescence, or capillary condensation, within a partially filled surface. However, in the present model, as a first approximation this difference is neglected, see also [76], and in the following "sorption isotherm" will be used with reference to both adsorption and desorption conditions.

The shape of the sorption isotherm for concrete is influenced by many factors, particularly those that influence the extent and rate of the chemical reactions and, in turn, determine pore structure and pore size distribution. These factors include water to cement ratio, cement chemical composition, silica fume content, curing time and method, temperature, and mix additives, etc.

In the literature, various formulations can be found to describe the sorption isotherm of normal concrete, see [77, 98]. In the present model, the semi-empirical expression proposed by Norling Mjornell [73] is adopted because it explicitly accounts for the evolution of hydration reaction and the SF content. The effect of the temperature on the sorption isotherm is considered by introducing an Arrhenius type corrective term. This sorption isotherm reads

$$w_e(h, T, \alpha_c, \alpha_s) = G_1(\alpha_c, \alpha_s) \left[1 - \frac{1}{e^{10(g_1 \alpha_c^\infty - \alpha_c)h}}\right] e^{\frac{Q}{R}\left(\frac{1}{T} - \frac{1}{T_0}\right)} + K_1(\alpha_c, \alpha_s) \left[e^{10(g_1 \alpha_c^\infty - \alpha_c)h} - 1\right] \tag{13}$$

where the first term (gel isotherm) represents the physically bound (adsorbed) water, which is corrected by the Arrhenius term $e^{Q/R(1/T - 1/T_0)}$, in order to account for the effect of temperature on the physically bound water, and the second term (capillary isotherm) represents the capillary water. The temperature

effect parameter Q/R is the activation energy, T_0 is the reference room temperature ($T_0 = 296K$). The material parameter $g_1 > 1$ governs the shape of the sorption isotherm.

In Eq. 13 the temperature effect is applied only to the term accounting for the evaporable water in the gel pores. In compliance with the conclusions drawn by several authors [99, 100, 101], the model aims to describe the phenomenon for which, under the same conditions, increasing temperature hinders adsorption and promotes desorption, resulting in a fewer number of water molecules that can be adsorbed. The opposite process is instead observed when the temperature decreases, i.e. more evaporable water is available under the same condition at a lower temperature.

The coefficient $G_1(\alpha_c, \alpha_s)$ represents the amount of water per unit volume held in the gel pores at 100% relative humidity, and it can be expressed [73] as

$$G_1(\alpha_c, \alpha_s) = k_{vg}^c \alpha_c c + k_{vg}^s \alpha_s s \tag{14}$$

where k_{vg}^c and k_{vg}^s are material parameters.

The maximum amount of water per unit volume, $w_e(h = 1, T, \alpha_c, \alpha_s)$, that can fill pores (both capillary pores and gel pores) at a certain degree of hydration under saturation conditions is given $w_0 - 0.188c\alpha_c + 0.22s\alpha_s$. By using this expression and the Eq. 13 with $h = 1$, and solving for $K_1(T, \alpha_c, \alpha_s)$ one obtains

$$K_1(T, \alpha_c, \alpha_s) = \frac{w_0 - 0.188\alpha_c c + 0.22\alpha_s s - G_1 \left[1 - e^{-10(g_1 \alpha_c^\infty - \alpha_c)}\right] e^{\frac{Q}{R}\left(\frac{1}{T} - \frac{1}{T_0}\right)}}{e^{10(g_1 \alpha_c^\infty - \alpha_c)} - 1} \tag{15}$$

The material parameters k_{vg}^c, k_{vg}^s, and g_1 can be calibrated by fitting experimental data relevant to free (evaporable) water content in concrete at various ages [73, 25].

3.5 Moisture permeability

Moisture transport in concrete depends on various diffusion mechanisms that characterize the mobility of different water phases present in concrete, and which are influenced by the pore structure of cement paste, such as molecular diffusion (ordinary diffusion), Knudsen diffusion, and surface diffusion [102, 103]. Although each individual mechanism is reasonably understood, it is not always easy to make an accurate prediction of the total diffusivity; it is difficult to describe and simulate the details of concrete pore structure formed by randomly oriented pores with variable pore radii and with varying degrees of tortuosity and connectivity. In addition, the scenario is further complicated by the dependence of the

pore structure on water to cement ratio, cement content, silica fume content, age, etc.

In this work, as typically done in literature [75], the above mechanisms are lumped and described phenomenologically through equivalent Fick's law (see Sec 2.2), characterized by the moisture permeability given by

$$D_h(h,T) = \psi(T) D_1 \left[1 + \left(\frac{D_1}{D_0} - 1 \right) (1-h)^n \right]^{-1} \quad \text{with} \quad \psi(T) = \exp\left(\frac{E_{ad}}{RT_0} - \frac{E_{ad}}{RT} \right) \tag{16}$$

In Eq. 16, the coefficient $\psi(T)$ takes into account the effect of temperature on permeability [104] as earlier proposed by Bažant [75], D_0 and D_1 represent moisture permeability for a completely dry situation ($h = 0$) and completely saturated situation ($h = 1$), respectively. The exponent n governs the rate at which permeability transitions from D_0 to D_1. In Eq. 16, T is the absolute temperature, T_0 is the reference room temperature ($T_0 = 296K$) and $E_{ad}/R \approx 2700K$ [75]. The material parameters D_0, D_1, and n can be calibrated by fitting experimental data relevant to moisture diffusion [25].

3.6 HTC formulation at the mesoscale

The heterogeneity considered in the FLM is the meso-scale heterogeneity related to the resolution scale of LDPM. Although, some authors use the term "meso-scale" in a wider sense to include concrete models targeting concrete a smaller scale. In FLM the 1D conduits are located and oriented according to the cement paste matrix distribution. This feature reflects ipso facto the discrepancy in the permeability of impermeable aggregates and permeable cement paste matrix. The FLM can capture the tortuosity of the flow network in the cementitious material given by the topological distribution of coarse aggregates. This means that FLM is able to account for the material heterogeneity but only at the mesoscale level, same scale (resolution) of LDPM. If the heterogeneities associated of smaller scale properties would be taken into account, they must be included in the HTC constitutive laws.

The implementation of the HTC model in the 3D FLM system paves the way for a new version of the formulation that can better exploit the features of the discrete mesoscale implementation. An update HTC formulation could be done by scaling all the properties (material parameters) based on the real cement paste content in the volume in each conduit (Flow Lattice Element). Another update would be a new calibration of the moisture diffusion parameters (D_0, D_1, and n) in order to reflect the mesoscale geometry (heterogeneity) of the fluid flow network after considering all the coarse aggregate particles in

the construction of the LDPM geometry. However, those updates and improvements are behind the scope of the manuscript and are left for future work.

The HTC formulation could be also improved by enhancing the mescoscale heterogeneity, which is considered in FLM since it is related to the resolution scale of LDPM, i.e. length scale 10^{-3} m. The heterogeneity can be extend at smaller scale, e.g. [105, 106], by a multi-scale approach by linking to the material porosity the HCT constitutive laws. However, this feature is also behind the scope of the manuscript.

4 Numerical implementation

In this work, the authors utilized a commercial finite element software *Abaqus* as the solver for the nonlinear system of equations, through the Abaqus user element subroutines for implicit analyses, named *UEL*. Generally, for a *UEL*, users should calculate the linearized governing equations (incremental form) for the nonlinear problems, by providing the Jacobian (a.k.a. the tangent stiffness) matrix *AMATRX* and the right hand side (a.k.a. the residual) vector *RHS* of the incremental governing equations to the Abaqus solver, to calculate the nodal increments of degrees of freedom for user elements during each iteration, until the convergence is reached. The remaining parts, such as matrix assemblage and matrix solving, are automatically processed by the Abaqus solver for implicit analyses *Abaqus/Standard*.

To calculate the incremental form for the HTC model within the FLE, one may rewrite the governing equations for the FLE, Eqs. 4, in a matrix form as

$$\mathbf{M}\dot{\mathbf{u}} + \mathbf{K}\mathbf{u} + \mathbf{S} = \mathbf{0} \tag{17}$$

where,

$$\mathbf{M} = V \begin{bmatrix} g_1 C_1 & 0 & 0 & 0 \\ 0 & g_1 C_3 & 0 & 0 \\ 0 & 0 & g_2 C_1 & 0 \\ 0 & 0 & 0 & g_2 C_3 \end{bmatrix} \tag{18}$$

$$\mathbf{K} = \frac{A}{l}\begin{bmatrix} D_h & 0 & -D_h & 0 \\ 0 & \lambda & 0 & -\lambda \\ -D_h & 0 & D_h & 0 \\ 0 & -\lambda & 0 & \lambda \end{bmatrix} \tag{19}$$

$$\mathbf{S} = V\begin{bmatrix} g_1 C_2 \; g_1 C_4 \; g_2 C_2 \; g_2 C_4 \end{bmatrix}^{\mathrm{T}} \tag{20}$$

$$\mathbf{u} = \begin{bmatrix} h_1 \; T_1 \; h_2 \; T_2 \end{bmatrix}^{\mathrm{T}} \tag{21}$$

in which, g_1 and g_2 are the length proportionality coefficients (see Sec. 2.1), the volumes are $V_1 = Vg_1$ and $V_2 = Vg_2$; the coefficients, which are estimated by the weighted averages of internal variables, read $D_h = D_h\left(h_1 g_2 + h_2 g_1, T_1 g_2 + T_2 g_1\right)$, $C_1 = \partial w_e/\partial h = g_2\left(\partial w_e/\partial h\right)|_1 + g_1\left(\partial w_e/\partial h\right)|_2$, $C_2 = g_2\left(\dot{q}_h\right)|_1 + g_1\left(\dot{q}_h\right)|_2$, $C_3 = \partial U/\partial T = \rho c_t = g_2\left(\rho c_t\right)|_1 + g_1\left(\rho c_t\right)|_2$, and $C_4 = g_2\left(\dot{q}_T\right)|_1 + g_1\left(\dot{q}_T\right)|_2$ where $\dot{q}_h = \partial w_e/\partial \alpha_c \cdot \dot{\alpha}_c + \partial w_e/\partial \alpha_s \cdot \dot{\alpha}_s + \dot{w}_n$ and $\dot{q}_T = \dot{\alpha_s}\; s\; \tilde{Q}_s^{\infty} + \dot{\alpha_c}\; c\; \tilde{Q}_c^{\infty}$. The subscripts 1 and 2 stand for the variables evaluated at node N_1 and N_2, respectively.

The above matrix form of the governing equations is nonlinear and is hard to be solved numerically. To linearize the nonlinear equations, one may rewrite Eq. 17 as: $\mathbf{f}\left(\mathbf{u}\right) = \mathbf{M}\dot{\mathbf{u}} + \mathbf{K}\mathbf{u} + \mathbf{S} = \mathbf{0}$. By adopting a root-finding algorithm, such as Newton-Raphson method (a.k.a. Newton's method) in this work, one may linearize the problem and approximate the nonlinear governing equations with the incremental form, which is given by

$$\begin{aligned} \mathbf{f}\left(\mathbf{u}_{n+1}\right) \approx \mathbf{f}\left(\mathbf{u}_n\right) + \frac{\partial \mathbf{f}\left(\mathbf{u}_n\right)}{\partial \mathbf{u}}\Delta\mathbf{u} = \mathbf{0} \\ \frac{\partial \mathbf{f}\left(\mathbf{u}_n\right)}{\partial \mathbf{u}}\Delta\mathbf{u} = -\mathbf{f}\left(\mathbf{u}_n\right) \end{aligned} \tag{22}$$

where the subscripts n and $n+1$ stand for the current and next iteration step for Newton's method

respectively, and

$$\mathbf{f}\left(\mathbf{u}\right)=\begin{bmatrix} f_1 \\ f_2 \\ f_3 \\ f_4 \end{bmatrix}=\begin{bmatrix} Vg_1C_1\dot{h}_1+\frac{A}{l}D_h\left(h_1-h_2\right)+Vg_1C_2 \\ Vg_1C_3\dot{T}_1+\frac{A}{l}\lambda\left(T_1-T_2\right)+Vg_1C_4 \\ Vg_2C_1\dot{h}_1-\frac{A}{l}D_h\left(h_1-h_2\right)+Vg_2C_2 \\ Vg_2C_3\dot{T}_1-\frac{A}{l}\lambda\left(T_1-T_2\right)+Vg_2C_4 \end{bmatrix} \tag{23}$$

The multiplier on the left-hand side of Eq. 22, $\partial\mathbf{f}\left(\mathbf{u}_n\right)/\partial\mathbf{u}$, is corresponding to the Jacobian matrix *AMATRX* and the term on the right-hand side $-\mathbf{f}\left(\mathbf{u}\right)$ is the right-hand side vector *RHS* in the Abaqus user element. The entries of the Jacobian matrix and the right-hand side vector corresponding to Eqs. 22 and 23 can be calculated by

$$\frac{\partial\mathbf{f}\left(\mathbf{u}_n\right)}{\partial\mathbf{u}}=\begin{bmatrix} \frac{\partial f_1}{\partial h_1} & 0 & \frac{\partial f_1}{\partial h_2} & 0 \\ 0 & \frac{\partial f_2}{\partial T_1} & 0 & \frac{\partial f_2}{\partial T_2} \\ \frac{\partial f_3}{\partial h_1} & 0 & \frac{\partial f_3}{\partial h_2} & 0 \\ 0 & \frac{\partial f_4}{\partial T_1} & 0 & \frac{\partial f_4}{\partial T_2} \end{bmatrix} \tag{24}$$

and

$$-\mathbf{f}\left(\mathbf{u}\right)=-\begin{bmatrix} f_1 & f_2 & f_3 & f_4 \end{bmatrix}^{\mathrm{T}} \tag{25}$$

The linearized governing equations are then assembled for all FLE control volumes and the assembly must be completed by appropriate boundary and initial conditions.

4.1 Time integration scheme

The backward Euler method is used in Abaqus/Standard for the time integration; it is unconditionally stable and allows large time increments. For the transient analysis of the HTC model, the backward Euler method is considered very effective, as the total simulation time is always extensive. Specifically, one can rewrite the governing equations 17 as

$$\mathbf{M}\dot{\mathbf{u}}+\mathbf{K}\mathbf{u}+\mathbf{S}\approx\mathbf{M}_{n+1}\frac{\mathbf{u}_{n+1}-\mathbf{u}_n}{\Delta t_{n+1}}+\mathbf{K}_{n+1}\mathbf{u}_{n+1}+\mathbf{S}_{n+1}=\mathbf{0} \tag{26}$$

In which the subscripts n and $n+1$ here represent the previous time step and the current time step. One may notice that the incremental form of the governing equations should take the partial derivatives at

the current time and that the matrices and the known term must be evaluated at the current time. The root-finding technique, i.e. the Newton-Raphson method, is then used for solving Eq. 22 for the FLM implementation.

Additionally, numerical implementation of the formulation in the previous sections requires, at the time integration of the internal variables, hydration degree and silica-fume reaction degree at each tet point of the flow lattice element mesh. The governing equations of the internal variables (Eqs. 5 and 7) can be all expressed in the form $\dot{x} = f(x, h, T)$, where x represent the internal variable. A very effective method to integrate these internal variables is the use of the second order Runge-Kutta formula (midpoint method) by which the value x_{n+1} of the internal variable at time t_{n+1} is given by $x_{n+1} \approx x_n + \Delta t_n f(x_{n+1/2}, h_{n+1/2}, T_{n+1/2})$; where x_n is the value of the internal variable at time t_n, Δt_n is the time increment, $x_{n+1/2} = (x_{n+1} + x_n)/2$, $h_{n+1/2} = (h_{n+1} + h_n)/2$, and $T_{n+1/2} = (T_{n+1} + T_n)/2$. All internal variables have zero value as an initial condition at the time $t_0 = 0$ (time of casting).

4.2 Boundary conditions

On the model boundaries, the mass and heat exchange between the concrete surface and the environment may be considered dependent not only on the conduction/diffusion, but also on the other mechanisms such as the heat convection and the phase change of water mass. In this study, one assumes the mass and heat exchange to be linearly dependent on the difference of surface relative humidity and environmental relative humidity, and the difference between surface temperature and environmental temperature, respectively.

A "boundary layer" (see Fig. 3) consisting of boundary layer (type 3) FLEs, as mentioned previously, extruding outwards from the concrete surface with prismatic volumes $V_1 = V_2 = V/2$, constant cross-section A, and lengths $l_1 = l_2 = l/2$, is added to the FLE network to simulate the water mass and heat exchange between the specimen and the environment at the specimen surface. All boundary layer FLEs are assumed to have the same material parameters of the FLEs which share the nodes on the specimen surface. In this way, the boundary conditions applied on the boundary layer are simplified to Dirichlet type conditions, $h_{bo} = h_{en}$, and $T_{bo} = T_{en}$, where, h_{bo} and T_{bo} are the relative humidity and the temperature of the extended boundary layer nodes; h_{en} and T_{en} are the relative humidity and the temperature of the environment. By varying the length of the boundary layer, one can simulate various degrees of surface emissivity.

5 Numerical simulations and comparisons with experimental data

5.1 Concrete drying

The first benchmark case for the calibration and validation of FLM focuses on the evolution of hydration degree and the spatial gradients of temperature and humidity fields in the case of the concrete moisture drying at early stages. The capability of FLM to capture the spatial gradients of temperature and humidity fields, as well as the capability of simulating the evolution of the hydration degree, is investigated by comparing FLM results with the reference experimental data of Kim and Lee [10]. The results were also compared with the HTC finite element implementation presented in Di Luzio and Cusatis [25].

Drying tests were conducted to observe the outward water mass flux at the boundaries due to the exposure of the concrete specimen to the ambient air with a smaller relative humidity, and the moisture diffusion inside the specimen due to the imbalance of relative humidity distribution from the core to the external surfaces. Self-desiccation also influences the entirety of the concrete drying process, predominately at early ages.

The drying test settings in Kim and Lee [10] are as illustrated in Fig. 4: prismatic concrete samples prepared with three mixes were exposed to ambient air with 50% relative humidity at one side, all other sides sealed to create an uniaxial moisture diffusion condition. The three mixes are categorized by their water-to-cement ratios, 0.28, 0.4, and 0.68. The corresponding mix compounds and concrete compositions for each category are found in [10]. The concrete specimens were moist-cured before drying, and the moisture distributions of specimens were measured at the sections spacing 3, 7, and 12 cm from the exposure surface, at two ages $t_0 = 3$ days and $t_0 = 28$ days. In addition to the drying specimens, variation in relative humidity due to self-desiccation only was also investigated via fully sealed concrete cubes with the same three mixes.

The continuous FEM simulations were performed with the finite element mesh as shown in Fig. 4a and FLM simulations with the mesh shown in Fig. 4b. It should be noticed that a boundary layer of FEM elements and FLE elements with the layer thickness of 1 mm was applied to the exposed surfaces of the respective models to properly reproduce the experimental conditions. The model parameters were adopted from [25], as these parameters captured accurately the self-desiccation experiments of water-cement-ratio $w/c = 0.4$ and age $t_0 = 3$ and $t_0 = 28$ days, as well as the drying experiments of water-cement-ratio $w/c = 0.4$ and age $t_0 = 3$ days. Table 1 summarizes the full list of model parameters used in the FLM

simulations.

Fig. 5a and b report the evolution of relative humidity vs. age for sealed concrete subjected to self-desiccation only after an initial curing of $t_0 = 3$ days and $t_0 = 28$ days. The results show that the relative humidity dropped after the initial curing, indicating that the water provided by moist-curing was not sufficient to maintain a fully saturated state. Furthermore, the concrete specimens with a low water-to-cement ratio tended to have a more significant drop in relative humidity, as expected.

The agreement of FLM simulation results with those of continuous FEM simulations and experimental data show that FLM can simulate accurately the drying test experiments. As required inputs for the drying test simulations, the initial hydration degree for mixes $w/c = 0.28$, $w/c = 0.4$, $w/c = 0.68$ due to self-desiccation were recorded as 0.3166, 0.3666, and 0.4323 at $t_0 = 3$ days and 0.4721, 0.5444, and 0.6376 at $t_0 = 28$ days, respectively. The initial hydration degree α_{c0} values are also reported in Tab. 1.

Fig. 6a, b and c show the experimental and numerical results of the relative humidity at multiple distances from the exposed surface for the drying tests, for an initial curing $t_0 = 3$ days. One can observe from the moisture transport in the concrete specimens at different ages that FLM captured well the gradient of relative humidity for various mixes by comparing to the experimental data and FEM simulation results. Moreover, the concretes with a low water-to-cement ratio dried quicker when compared to ones with higher water-to-cement ratios. The high initial relative humidity for high water-to-cement ratio concretes and the slightly lower initial relative humidity for low water-to-cement ratio concrete also suggest the correct modeling of initial curing for these drying test specimens. Similar observations can be concluded from the experimental and numerical results for drying tests of different mixes with initial curing $t_0 = 28$ days in Fig. 7a, b and c.

By comparing the results of self-desiccation tests and drying tests in Fig. 5, Fig. 6 and Fig. 7, one observes that self-desiccation is the predominant cause of the decrease in relative humidity when the water-to-cement ratios of specimens are low, and moisture transport is the predominant cause when water-to-cement ratios are high. This observation is in accordance with known behavior, where concrete with low water-to-cement ratios tends to form a denser microstructure and consequently consumes more water during hydration. The overall results of FLM simulations validate the capability of FLM for capturing self-desiccation, as well as the moisture transport procedure in various concrete mixes.

Table 1: Model parameters used in numerical simulations in Section 5

Parameter [unit]	**Section 5.1 and 5.2**	**Section 5.3**
ρ [kg/m^3]	2500	2400
w/c [-]	0.28/0.40/0.68	0.25
c [kg/m^3]	541/423/310	748
κ [W/m/K]	2.5	2.5
c_t [J/K/kg]	1100	1100
A_{c1} [1/s]	4166.5	55600.0
A_{c2} [-]	5.00E-02	1.00E-04
η_c [-]	8.0	8.0
E_{ac}/R [K]	5000	5000
a [-]	5.5	5.5
b [-]	4.0	4.0
$\tilde{Q}_c^\infty$ [J/kg]	5.00E+05	5.00E+05
D_0 [kg/m/s]	2.80E-10/6.39E-10/2.30E-09	6.00E-10
D_1 [kg/m/s]	3.73E-08/7.12E-08/1.97E-07	1.00E-07
n [-]	3.0	4.0
E_{ad}/R [K]	2700	840
T_{ref} [°C]	23.00	20.00
k_{vg}^c [-]	0.255	0.220
g_1 [-]	1.2	1.1
κ_c [-]	0.253	0.185
s [kg/m^3]	0.0	224.3
$\tilde{Q}_s^\infty$ [J/kg]	0.0	7.80E+05
E_{as}/R [K]	0.0	9700
A_{s1} [1/s]	0.0	1.39E+10
A_{s2} [-]	0.0	1.00E-06
η_s [-]	0.0	9.5
k_{vg}^s [-]	0.0	0.36
SF^{eff} [-]	0.0	1.0
α_{c0} [-] (initial hydration degree)	3days 0.3166/0.3666/0.4323 28days 0.4721/0.5444/0.6376	0.0
Q/R [K]	0.0	1500

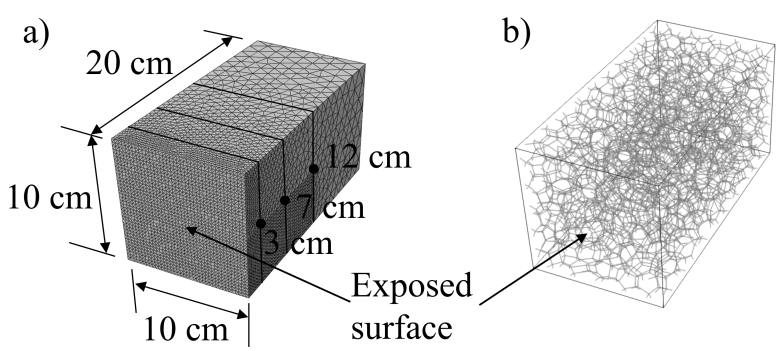

Figure 4: Experimental and numerical setups of drying tests of Kim and Lee [10]: a) dimensions of the specimen and the finite element mesh, b) FLM mesh

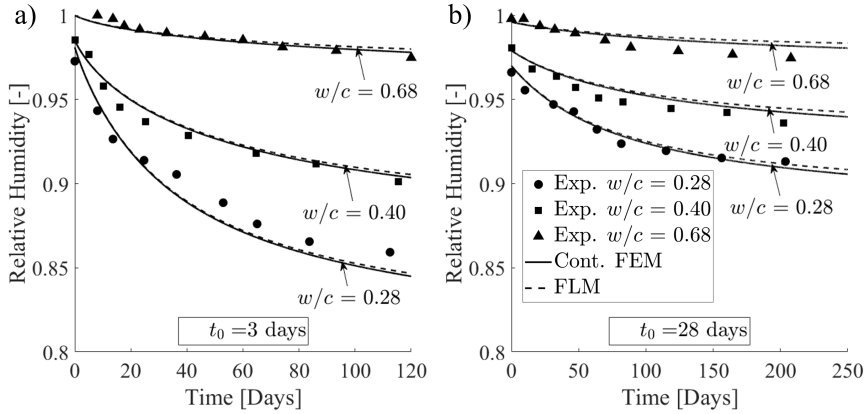

Figure 5: Numerical simulations of the experimental data of Kim and Lee [10]: relative humidity vs. age due to self-desiccation only, for a) $t_0 = 3$ days, and b) $t_0 = 28$ days

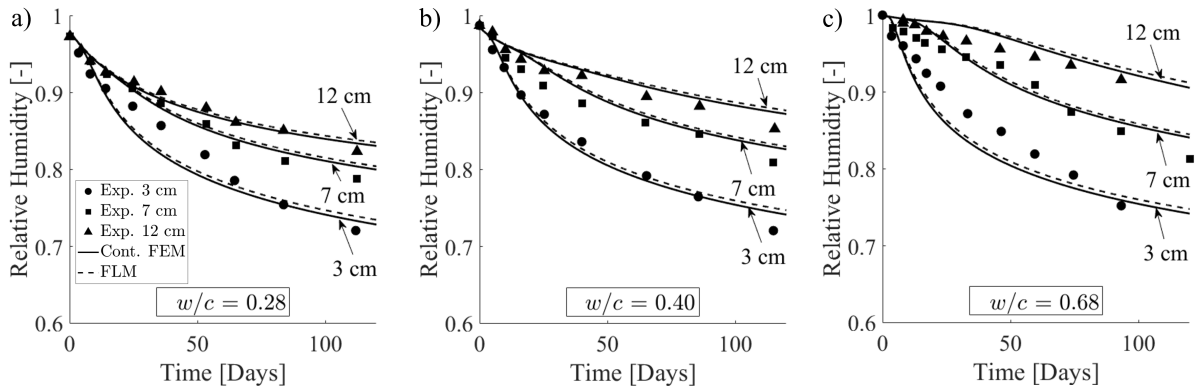

Figure 6: Numerical simulations of the experimental data of Kim and Lee [10]: relative humidity vs. age at different sections from the exposed surface of concrete specimens due to drying and self-desiccation for $t_0 = 3$ days, with a) mix $w/c = 0.28$, b) mix $w/c = 0.40$, and c) mix $w/c = 0.68$

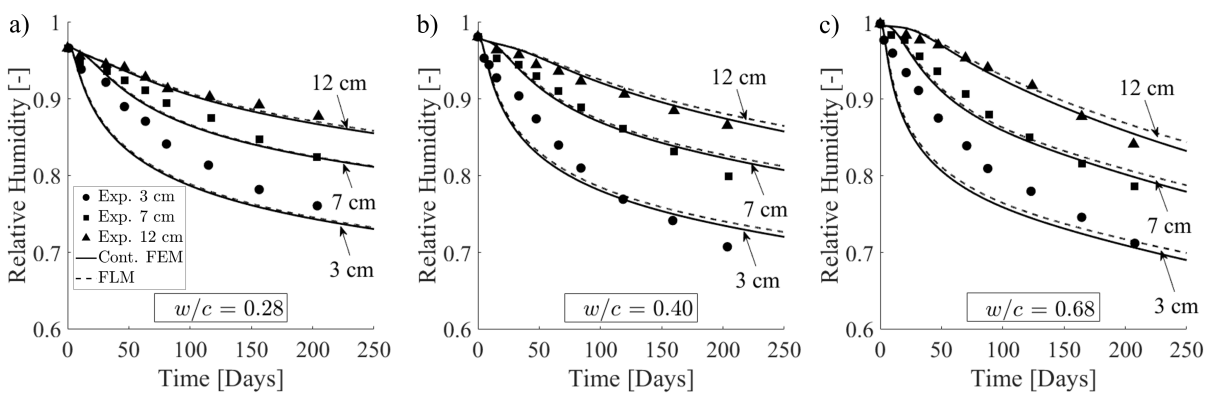

Figure 7: Numerical simulations of the experimental data of Kim and Lee [10]: relative humidity vs. age at different sections from the exposed surface of concrete specimens due to drying and self-desiccation for $t_0 = 28$ days, with a) mix $w/c = 0.28$, b) mix $w/c = 0.40$, and c) mix $w/c = 0.68$

5.2 Temperature-dependent desorption isotherm

In the previous section, the overall agreement regarding the water diffusion, as well as self-desiccation results with experimental data, show that FLM has the capability to capture moisture transport in drying tests of concrete with various water-to-cement ratios. Yet, the verification of FLM to capture hydration evolution and moisture transport under different temperatures is still needed. In this section, the formulation of the temperature-dependent sorption isotherm presented in the previous Sec. 3.4 is first verified. For this purpose, the desorption tests of 3.6 years-old mortar ($w/c = 0.50$) with reference to the experimental data of Hundt and Kantelberg [107] are here considered, to calibrate the activation energy Q/R within the temperature dependent term in Eq. 13.

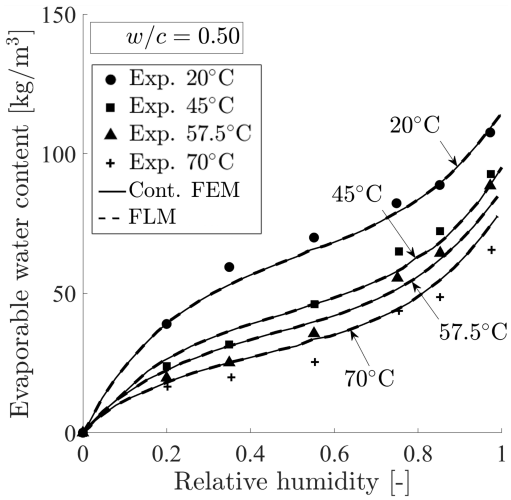

Figure 8: Calibration of the sorption law against the experimental isotherms of Hundt and Kantelberg [107]: evaporable water content vs. relative humidity at various room temperatures, in mortar specimens with mix $w/c = 0.50$

The calibration is accomplished by looking for the best match between the experimental isotherms and the numerical simulation results returned by the employment of the HTC sorption law in Eq. 13. The good agreement between numerical and laboratory outcomes is achieved with $Q/R = 1500K$, see Fig. 8. The model capability of capturing the experimental trends demonstrates the effectiveness of the approach adopted to account for the temperature effect on the variation of the evaporable water content.

5.3 Concrete drying at early-age

In this section drying tests on Ultra High Performance Concrete (UHPC) with reference to the experimental data of Soliman [108] are considered.

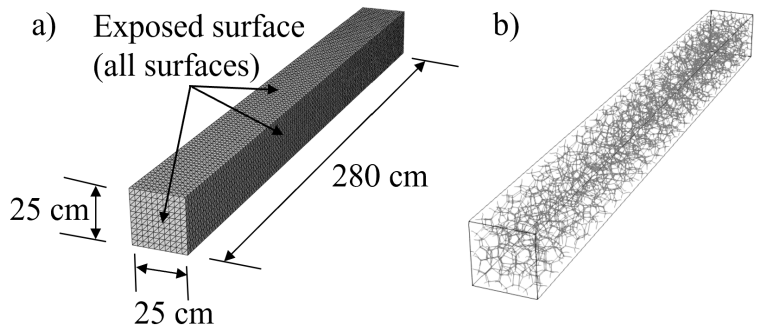

Figure 9: Experimental and numerical setups of drying tests of Soliman [108]: a) dimensions of the specimen and the finite element mesh, b) FLM mesh

The specimen settings in Soliman [108] are, as illustrated in Fig. 9a. Prismatic concrete specimens with dimensions 25 mm $\times$ 25 mm $\times$ 280 mm were dried at all surfaces exposed to the ambient conditions. All specimens were taken from a single batch and, after casting, were maintained at a room temperature (20 ± 1°C) and covered with polyethylene sheets until demolding to avoid moisture loss. All specimens were demolded at the final setting time and initial readings were taken before moving specimens to the pre-determined curing conditions: 10°C, 20°C, and 40°C, and ambient air with 40%, 60%, and 80% relative humidity. All surfaces of the specimens were at the same temperature and relative humidity. In the experimental investigation the authors measured the mass loss of the specimens and the evolution of hydration degree under sealed conditions at different temperatures. The investigated mix features a water-to-cement ratio w/c equal to 0.25; the corresponding mix design and concrete composition is found in [108] and also listed in Tab. 1.

The FEM mesh and FLM mesh are shown in Fig. 9a and b, respectively. Exposed surfaces (all surfaces) of the respective models were covered by a boundary layer of FEM and FLM elements with the thickness of 1 mm. Model parameters for hydration were firstly calibrated using the experimental data from sealed tests at 10°C, 20°C, 40°C. Then, the permeability parameters were calibrated from the drying tests at temperatures 20°C and 40°C with ambient air relative humidity of 60%. The full list of model parameters used in the simulations in this section can be found in Tab. 1. All remaining curves are model predictions.

Fig. 10 reports the evolution of the hydration degree vs. age for experiments and numerical simulations. The agreement between numerical results and experimental data shows that FLM simulated the cement hydration behaviors of UHPC accurately. The numerical results of the water loss tests are reported in Fig. 11 showing an overall sufficient fitting of the experimental data. Some differences appear

in the simulations of the tests at 10° C, and at 40° C with 80% relative humidity, although by means of the Arrhenius type corrective terms, the HTC formulation appears to have the capability of capturing experimental trends.

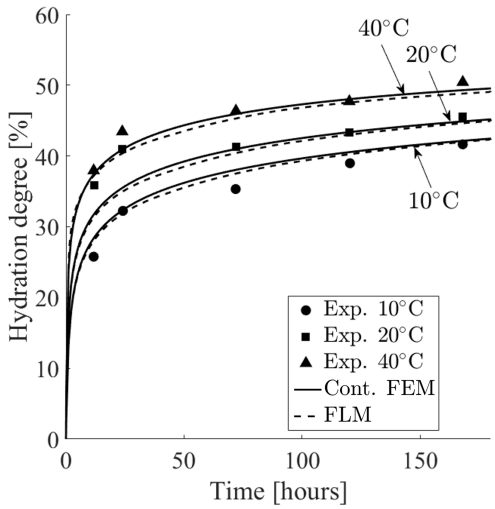

Figure 10: Numerical simulations of the experimental data of Soliman [108]: hydration degree vs. age due to self-desiccation only, in concrete specimens with mix $w/c = 0.25$ at various room temperatures

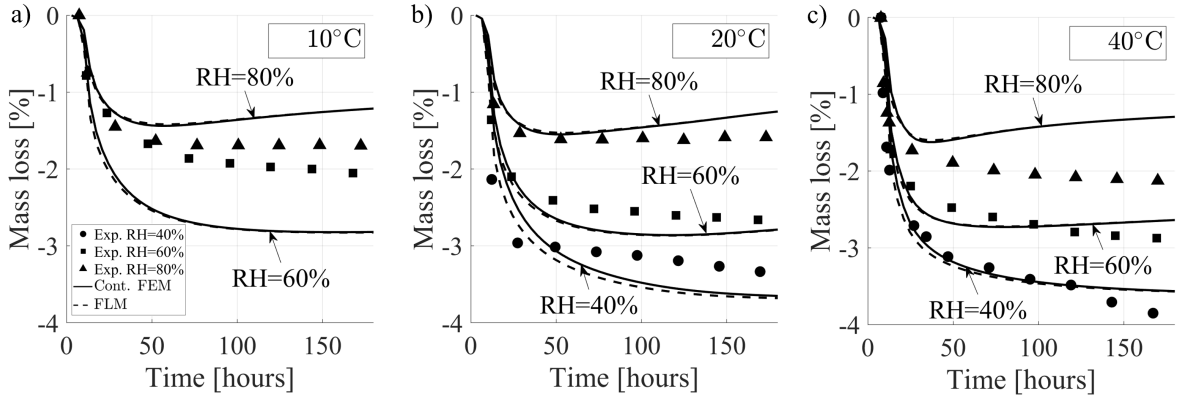

Figure 11: Numerical simulations of the experimental data of Soliman [108]: water loss vs. age due to drying and self-desiccation in concrete mix $w/c = 0.25$ specimens at various ambient temperatures, a) $T = 10°$, b) $T = 20°$, and c) $T = 40°$

By increasing the temperature from 10° C to 40° C, competing phenomena are triggered. On one hand, the hydration process is accelerated, thus self-desiccation is increased as less water available for the diffusion. On the other hand, at higher temperatures fewer water molecules are adsorbed by the walls of the gel pores, resulting in lower availability of water for feeding the aging reactions. In this case, a lower consumption of water is expected. The process is further complicated by drying due to

the imbalance between the inner moisture content and the environmental relative humidity, a process which is highly dependent on temperature. The experiments show that moisture loss increases when temperature increases, particularly in drier environments (i.e. 60% and 40% in Fig. 11). This trend is less clear when material aging occurs at higher relative humidity (i.e. 80% in Fig. 11). The model simulates with sufficient accuracy the material behavior at 20° C and 40° C, whereas it overestimates the variation in moisture loss between the responses at 10° C with relative humidity equals to 80% and 60%. This discrepancy between the experimental study and the numerical methods can be explained by the fact that the temperature dependence of the sorption isotherm and of the diffusion coefficient (for which no experimental data were available for this experimental data [108]) seems not capturing very well the temperature variations being the tests at 20° C simulated sufficiently well. Without a doubt, this feature of model needs further future validation with a comprehensive experimental data in which additional data would be available (e.g. sorption isotherm and diffusion coefficient at different temperatures) not only the hydration evolution at different temperatures as for [108].

6 Conclusions and future work

In this study, a 3D Flow Lattice Model (FLM) with the application to the Hygro-Thermo-Chemical (HTC) model [24, 25] has been formulated, for the simulation of moisture transport and heat transfer in cementitious materials. FLM utilized the topology of the Lattice Discrete Particle Model (LDPM) for the construction of the Flow Lattice Element (FLE) network, and the governing equations of FLE have been derived through the mass and enthalpy conservation laws. The numerical implementation of FLM is implemented via Abaqus user element subroutines *UEL*.

The implemented FLM has been validated using a large set of experimental data available in the literature. The results show the following conclusions:

1. FLM can simulate and predict with high accuracy the moisture variation in self-desiccation and drying experiments for a wide range of standard and high-performance concrete mixes.

2. The FLM implementation of HTC sorption laws, enriched with the Arrhenius temperature-dependent term, can simulate with sufficient accuracy the effect of temperature on the variation of the evaporable water content.

3. Implementation in the LDPM framework in part develops an enhanced Multiphysics-Lattice Discrete Particle Model (M-LDPM) framework which may be used for computational analysis of frac-

ture permeability behavior of cementitious materials.

FLM, combined with the dual lattice topology, enables the seamless coupling of the mechanical and diffusion/chemical behavior of the material at the aggregate scale. As a consequence, the variation of the conductivity/permeability induced by fracturing processes can be simulated by relating the transport properties of flow elements with local cracking behaviors. However, this is beyond the purpose of this paper and it will be discussed in subsequent work.

Acknowledgements

This manuscript has been authored in part by UT-Battelle, LLC, under contract DE-AC05-00OR22725 with the US Department of Energy (DOE). The publisher acknowledges the US government license to provide public access under the DOE Public Access Plan (http://energy.gov/downloads/doe-public-access-plan).

The authors confirm that the data supporting the findings of this study are available within the article and its supplementary materials.

References

[1] Falikman Vyatcheslav, Realfonzo Roberto, Coppola Luigi, Hàjek Petr, and Riva Paolo, eds. *Durability and Sustainability of Concrete Structures (DSCS-2018)*. ACI, SP-326, 2018. ISBN: 9781641950220.

[2] Junquan Li, Zemei Wu, Caijun Shi, Qiang Yuan, and Zuhua Zhang. "Durability of ultra-high performance concrete – A review". In: *Construction and Building Materials* 255 (2020), p. 119296. ISSN: 0950-0618.

[3] Trevor Looney, Maranda Leggs, Jeffery Volz, and Royce Floyd. "Durability and corrosion resistance of ultra-high performance concretes for repair". In: *Construction and Building Materials* 345 (2022), p. 128238. ISSN: 0950-0618.

[4] Dejian Shen, Jinliang Jiang, Jiaxin Shen, Panpan Yao, and Guoqing Jiang. "Influence of curing temperature on autogenous shrinkage and cracking resistance of high-performance concrete at an early age". In: *Construction and Building Materials* 103 (2016), pp. 67–76. ISSN: 0950-0618.

[5] C Hua, P Acker, and A Ehrlacher. "Analyses and models of the autogenous shrinkage of hardening cement paste: I. Modelling at macroscopic scale". In: *Cement and Concrete Research* 25.7 (1995), pp. 1457–1468.

[6] Bertil Persson. "Self-desiccation and its importance in concrete technology". In: *Materials and Structures* 30.5 (1997), pp. 293–305.

[7] Lars-Olof Nilsson and Kristina Mjörnell. "A Micro-model for Self-desiccation in High Performance Concrete". In: *Proceedings of the Fourth International Research Seminar, Gaithersburg, Maryland, USA*. 2005.

[8] Hui Chen, Mateusz Wyrzykowski, Karen Scrivener, and Pietro Lura. "Prediction of self-desiccation in low water-to-cement ratio pastes based on pore structure evolution". In: *Cement and Concrete Research* 49 (2013), pp. 38–47.

[9] F. H. Wittmann. "Crack formation and fracture energy of normal and high strength concrete". In: *Sādhanā* 27.4 (2002), pp. 413–423.

[10] Jin-Keun Kim and Chil-Sung Lee. "Moisture diffusion of concrete considering self-desiccation at early ages". In: *Cement and Concrete Research* 29.12 (1999), pp. 1921–1927.

[11] T Knudsen. "Modeling hydration of Portland cementâ€"the effect of particle size distribution". In: *Proceedings of the engineering foundation conference on characterization and performance prediction of cement and concrete*. 1982.

[12] Dale P Bentz. "Influence of water-to-cement ratio on hydration kinetics: simple models based on spatial considerations". In: *Cement and Concrete Research* 36.2 (2006), pp. 238–244.

[13] F. J. Ulm and O. Coussy. "Modeling of thermo-chemo-mechanical couplings of concrete at early ages". In: *Journal of Engineering Mechanics* 121.7 (1995), pp. 785–794.

[14] Geert De Schutter and Luc Taerwe. "Degree of hydration-based description of mechanical properties of early age concrete". In: *Materials and Structures* 29.6 (1996), p. 335.

[15] M. Cervera, J. Oliver, and T. Prato. "Thermo-chemo-mechanical model for concrete. I: Hydration and aging". In: *Journal of Engineering Mechanics* 125.9 (1999), pp. 1018–1027.

[16] Zhishan Zheng and Xiaosheng Wei. "Mesoscopic models and numerical simulations of the temperature field and hydration degree in early-age concrete". In: *Construction and Building Materials* 266 (2021), p. 121001. ISSN: 0950-0618.

[17] Dejian Shen, Ci Liu, Mingliang Wang, Xingcan Jin, and Hui Tang. "Prediction model for internal relative humidity in early-age concrete under different curing humidity conditions". In: *Construction and Building Materials* 265 (2020), p. 119987. ISSN: 0950-0618.

[18] D. Gawin, F. Pesanto, and B. A. Schrefler. "Hygro-thermo-chemo-mechanical modelling of concrete at early ages and beyond. Part I: hydration and hygro-thermal phenomena". In: *International Journal for Numerical Methods in Engineering* 67.3 (2006), pp. 299–331.

[19] Dariusz Gawin, Francesco Pesavento, and Bernhard Schrefler. "Hygro-thermo-chemo-mechanical modelling of concrete at early ages and beyond. Part II: shrinkage and creep of concrete". In: *International Journal for Numerical Methods in Engineering* 67.3 (2006), pp. 332–363.

[20] Feng Lin and Christian Meyer. "Hydration kinetics modeling of Portland cement considering the effects of curing temperature and applied pressure". In: *Cement and Concrete Research* 39.4 (2009), pp. 255–265.

[21] Saeed Rahimi-Aghdam, Zdeněk P Bažant, and MJ Abdolhosseini Qomi. "Cement hydration from hours to centuries controlled by diffusion through barrier shells of CSH". In: *Journal of the Mechanics and Physics of Solids* 99 (2017), pp. 211–224.

[22] Yaming Pan et al. "Lattice modeling of early-age behavior of structural concrete". In: *Materials* 10.3 (2017), p. 231.

[23] Lei Shen, Huayi Zhang, Giovanni Di Luzio, Hao Yin, Lifu Yang, and Gianluca Cusatis. "Mesoscopic discrete modeling of multiaxial load-induced thermal strain of concrete at high temperature". In: *International Journal of Mechanical Sciences* 232 (2022), p. 107613.

[24] Giovanni Di Luzio and Gianluca Cusatis. "Hygro-thermo-chemical modeling of high performance concrete. I: Theory." In: *Cement and Concrete Composites* 31.5 (2009), pp. 301–308.

[25] Giovanni Di Luzio and Gianluca Cusatis. "Hygro-thermo-chemical modeling of high performance concrete. II: Numerical implementation, calibration, and validation." In: *Cement and Concrete Composites* 31.5 (2009), pp. 309–324.

[26] J.A. Teixeira de Freitas, P.T. Cuong, and Faria Rui. "Modeling of cement hydration in high performance concrete structures with hybrid finite elements". In: *International Journal for Numerical Methods in Engineering* 103.5 (2015), pp. 364–390.

[27] I Boumakis, M Marcon, Lin Wan, and R Wendner. "Creep and shrinkage in fastening systems". In: *CONCREEP 10*. ASCE, 2015, pp. 657–666.

[28] Massimiliano Bocciarelli and Gianluca Ranzi. "Identification of the hygro-thermo-chemical-mechanical model parameters of concrete through inverse analysis". In: *Construction and Building Materials* 162 (2018), pp. 202–214.

[29] Massimiliano Bocciarelli and Gianluca Ranzi. "An inverse analysis approach for the identification of the hygro-thermo-chemical model parameters of concrete". In: *International Journal of Mechanical Sciences* 138 (2018), pp. 368–382.

[30] I. Boumakis, G. Di Luzio, M. Marcon, J. Vorel, and R. Wan-Wendner. "Discrete element framework for modeling tertiary creep of concrete in tension and compression". In: *Engineering Fracture Mechanics* 200 (2018), pp. 263–282. ISSN: 0013-7944.

[31] G. Di Luzio, L. Ferrara, and V. Krelani. "Numerical modeling of mechanical regain due to self-healing in cement based composites". In: *Cement and Concrete Composites* 86 (2018), pp. 190–205. ISSN: 0958-9465. DOI: `https://doi.org/10.1016/j.cemconcomp.2017.11.006`.

[32] Jan Eliáš, Hao Yin, and Gianluca Cusatis. "Homogenization of discrete diffusion models by asymptotic expansion". In: *International Journal for Numerical and Analytical Methods in Geomechanics* (2022).

[33] M. Pathirage, D.P. Bentz, G. Di Luzio, E. Masoero, and G. Cusatis. "The ONIX model: a parameter-free multiscale framework for the prediction of self-desiccation in concrete". In: *Cement and Concrete Composites* 103 (2019), pp. 36–48.

[34] Dale P Bentz and Edward J Garboczi. "Digitised simulation model for microstructural development". In: *Ceram. Trans.* 16 (1990), pp. 211–226.

[35] Dale P Bentz. "Three-dimensional computer simulation of Portland cement hydration and microstructure development". In: *Journal of the American Ceramic Society* 80.1 (1997), pp. 3–21.

[36] J. Ožbolt, G. Balabanic, G. Periškic, and M. Kušter. "Modelling the effect of damage on transport processes in concrete". In: *Construction and Building Materials* 24.9 (2010), pp. 1638–1648.

[37] S. Roels, P. Moonen, K. de Proft, and J. Carmeliet. "A coupled discrete-continuum approach to simulate moisture effects on damage processes in porous materials." In: *Comput. Methods Appl. Mech. Eng.* 195 (2006), pp. 7139–7153.

[38] J.M. Segura and I. Carol. "Coupled HM analysis using zero-thickness interface elements with double nodes—Part I: Theoretical model." In: *Int. J. Numer. Anal. Methods Geomech.* 32 (2008), pp. 2083–2101.

[39] B. Carrier and S. Granet. "Numerical modeling of hydraulic fracture problem in permeable medium using cohesive zone model." In: *Eng. Fract. Mech.* 79 (2012), pp. 312–328.

[40] Y. Yao, L. Li, and L. Keer. "Pore pressure cohesive zone modeling of hydraulic fracture in quasi-brittle rocks." In: *Mech. Mater.* 83 (2015), pp. 17–29.

[41] G. Chatzigeorgiou, V. Picandet, A. Khelidj, and G. Pijaudier-Cabot. "Coupling between progressive damage and permeability of concrete: analysis with a discrete model." In: *Int. J. Numer. Anal. Methods Geomech.* 29 (2005), pp. 1005–1018.

[42] H. Nakamura, W. Srisoros, R. Yashiro, and M. Kunieda. "Time-dependent structural analysis considering mass transfer to evaluate deterioration process of RC structures." In: *J. Adv. Concr. Technol.* 4 (2006), pp. 147–158.

[43] L. Wang, M. Soda, and T. Ueda. "Simulation of chloride diffusivity for cracked concrete based on RBSM and truss network model." In: *J. Adv. Concr. Technol.* 6 (2008), pp. 143–155.

[44] B. Šavija, J. Pacheco, and E. Schlangen. "Lattice modeling of chloride diffusion in sound and cracked concrete." In: *Cem. Concr. Compos.* 42 (2013), pp. 30–40.

[45] D. Asahina, J.E. Houseworth, J.T. Birkholzer, J. Rutqvist, and J.E. Bolander. "Hydro-mechanical model for wetting/drying and fracture development in geomaterials." In: *Comput. Geosci.* 65 (2014), pp. 13–23.

[46] S. Marina, I. Derek, P. Mohamed, S. Yong, and E.K. Imo-Imo. "Simulation of the hydraulic fracturing process of fractured rocks by the discrete element method." In: *Environ. Earth Sci.* 73 (2015), pp. 8451–8469.

[47] B. Damjanac, C. Detournay, and P.A. Cundall. "Application of particle and lattice codes to simulation of hydraulic fracturing." In: *Comput. Part. Mech.* (2015), pp. 1–13.

[48] J.E. Bolander and S. Berton. "Simulation of shrinkage induced cracking in cement composite overlays." In: *Cem. Concr. Compos.* 26 (2004), pp. 861–871.

[49] Peter Grassl and John Bolander. "Three-Dimensional Network Model for Coupling of Fracture and Mass Transport in Quasi-Brittle Geomaterials". In: *Materials* 9.9 (2016).

[50] Y. Zhang, G. Di Luzio, and M. Alnaggar. "Coupled multi-physics simulation of chloride diffusion in saturated and unsaturated concrete". In: *Construction and Building Materials* 292 (2021), p. 123394. ISSN: 0950-0618.

[51] G. Cusatis, D. Pelessone, and A. Mencarelli. "Lattice Discrete Particle Model (LDPM) for Concrete failure Behavior of Concrete. I: Theory". In: *Cement and Concrete Composites* 33.9 (2011), pp. 881–890.

[52] G. Cusatis, A. Mencarelli, D. Pelessone, and J.T. Baylot. "Lattice Discrete Particle Model (LDPM) for Failure Behavior of Concrete. II: Calibration and Validation". In: *Cement and Concrete Composites* 33.9 (2011), pp. 891–905.

[53] Edward A Schauffert and Gianluca Cusatis. "Lattice discrete particle model for fiber-reinforced concrete. I: Theory". In: *Journal of Engineering Mechanics* 138.7 (2011), pp. 826–833.

[54] Edward A Schauffert, Gianluca Cusatis, Daniele Pelessone, James L O'Daniel, and James T Baylot. "Lattice discrete particle model for fiber-reinforced concrete. II: tensile fracture and multiaxial loading behavior". In: *Journal of Engineering Mechanics* 138.7 (2011), pp. 834–841.

[55] Congrui Jin, Nicola Buratti, Marco Stacchini, Marco Savoia, and Gianluca Cusatis. "Lattice discrete particle modeling of fiber reinforced concrete: Experiments and simulations". In: *European Journal of Mechanics-A/Solids* 57 (2016), pp. 85–107.

[56] G Cusatis, Roozbeh Rezakhani, M Alnaggar, X Zhou, and D Pelessone. "Multiscale computational models for the simulation of concrete materials and structures". In: *Computational Modelling of Concrete Structures* 1 (2014), pp. 23–38.

[57] M Pathirage, F Bousikhane, M D'Ambrosia, M Alnaggar, and G Cusatis. "Effect of alkali silica reaction on the mechanical properties of aging mortar bars: Experiments and numerical modeling". In: *International Journal of Damage Mechanics* 28.2 (2019), pp. 291–322.

[58] Shady Gomaa, Tathagata Bhaduri, and Mohammed Alnaggar. "Coupled Experimental and Computational Investigation of the Interplay between Discrete and Continuous Reinforcement in Ultra-high Performance Concrete Beams. I: Experimental Testing". In: *Journal of Engineering Mechanics* 147.9 (2021), p. 04021049.

[59] Tathagata Bhaduri, Shady Gomaa, and Mohammed Alnaggar. "Coupled Experimental and Computational Investigation of the Interplay between Discrete and Continuous Reinforcement in Ultra-high Performance Concrete Beams. II: Mesoscale Modeling". In: *Journal of Engineering Mechanics* 147.9 (2021), p. 04021050.

[60] Mohammed Abdellatef and Mohammed Alnaggar. "Energy-Based Coarse Graining of the Lattice-Discrete Particle Model". In: *Journal of Engineering Mechanics* 146.5 (2020), p. 04020026.

[61] Weixin Li, Xinwei Zhou, J William Carey, Luke P Frash, and Gianluca Cusatis. "Multiphysics lattice discrete particle modeling (M-LDPM) for the simulation of shale fracture permeability". In: *Rock Mechanics and Rock Engineering* 51.12 (2018), pp. 3963–3981.

[62] Lei Shen, Weixin Li, Xinwei Zhou, Jun Feng, Giovanni Di Luzio, Qingwen Ren, and Gianluca Cusatis. "Multiphysics Lattice Discrete Particle Model for the simulation of concrete thermal spalling". In: *Cement and Concrete Composites* 106 (2020), p. 103457.

[63] Lifu Yang, Madura Pathirage, Huaizhi Su, Mohammed Alnaggar, Giovanni Di Luzio, and Gianluca Cusatis. "Computational modeling of expansion and deterioration due to alkali-silica reaction: Effects of size range, size distribution, and content of reactive aggregate". In: *International Journal of Solids and Structures* (2021), p. 111220.

[64] Lifu Yang, Madura Pathirage, Huaizhi Su, Mohammed Alnaggar, Giovanni Di Luzio, and Gianluca Cusatis. "Computational modeling of temperature and relative humidity effects on concrete expansion due to alkali-silica reaction". In: *Cement and Concrete Composites* (2021), p. 104237.

[65] Jan Eliáš and Gianluca Cusatis. "Homogenization of discrete mesoscale model of concrete for coupled mass transport and mechanics by asymptotic expansion". In: *Journal of the Mechanics and Physics of Solids* 167 (2022), p. 105010. ISSN: 0022-5096. DOI: https://doi.org/10.1016/j.jmps.2022.105010. URL: https://www.sciencedirect.com/science/article/pii/S0022509622001971.

[66] Antonio Cibelli, Madura Pathirage, Gianluca Cusatis, Liberato Ferrara, and Giovanni Di Luzio. "A discrete numerical model for the effects of crack healing on the behaviour of ordinary plain concrete: Implementation, calibration, and validation". In: *Engineering Fracture Mechanics* 263 (2022), p. 108266. ISSN: 0013-7944. DOI: https://doi.org/10.1016/j.engfracmech.2022.108266. URL: https://www.sciencedirect.com/science/article/pii/S0013794422000339.

[67] T. C. Powers and T. L. Brownyard. "Physical Properties of Hardened Cement Paste". In: *ACI Journal, Proceedings* 18.3 (1946), pp. 250–336.

[68] T. C. Powers. "Chemistry of Cements". In: Academic Press, London, 1964. Chap. Physical Structure of Portland Cement Paste, pp. 391–416.

[69] ZP Bažant. "Constitutive equation for concrete creep and shrinkage based on thermodynamics of multiphase systems". In: *Matériaux et Construction* 3.1 (1970), pp. 3–36.

[70] J. Claesson. *Few remarks on moisture flow potential.* Report TVBH-7163. Division of building physics, Lund Institute of Thecnology, 1993.

[71] R. H. Mills. *Factors influencing cessation of hydration in water-cured cement pastes.* Special report n. 90. Proceding of the Symposium on the structure of Portland Cement paste and concrete, Highway reaserch board, Washington D.C., 1966, pp. 406–424.

[72] S.J. Pantazopoulo and R.H. Mills. "Microstructural aspects of the mechanical response of plain concrete". In: *ACI Matererials journal* 92.6 (1995), pp. 605–616.

[73] K. Norling Mjonell. "A model on self-desiccation in high-performance concrete". In: *Self-desiccation and its importance in concrete technology Proceedings of the International Research Seminar.* Lund, Sweden, 1997, pp. 141–157.

[74] A.M. Neville. *Properties of Concrete.* New York: John Wiley and Sons, 1997.

[75] Z.P. Bažant. "Prediction of concrete creep effects using age-adjusted effective modulus method." In: *J. Am. Concr. Inst.* 69 (1972), pp. 212–217.

[76] Y. Xi, Z.P. Bažant, and H.M. Jennings. "Moisture diffusion in cementitious materials–Adsorption isotherms". In: *Advanced cement based materials* 1 (1994), pp. 248–257.

[77] Zdeněk P Bažant and Milan Jirásek. *Creep and hygrothermal effects in concrete structures.* Vol. 38. Springer, 2018.

[78] DP. Bentz and PE. Stutzman. "SEM analysis and computer modelling of hydration of Portland cement particles." In: *In Petrography of Cementitious Materials, ASTM STP 1215.* Ed. by de Hayes SM and Stark D. Vol. 225. Philadelphia, USA: ASTM, 1994, 27–76, with discussion 76–130.

[79] L. Taerwe G. de Schutter. "General hydration model for portland cement and blast furnace slag cement". In: *Cement and Concrete Research* 25 (1995), pp. 593–604.

[80] DP. Bentz, V. Waller, and F. De Larrard. "Prediction of adiabatic temperature rise in conventional and high-performance concretes using a 3-D microstructural model". In: *Cement and Concrete Research* 28.2 (1998), pp. 285–297.

[81] V Waller, F De Larrard, P Roussel, et al. "Modelling the temperature rise in massive HPC structures". In: *4th International Symposium on Utilization of High-Strength/High-Performance Concrete.* RILEM SARL Paris. 1996, pp. 415–421.

[82] H.F.W. Taylor. *Cement Chemistry.* London: Thomas Telford, 1997.

[83] K. van Breugel. “Numerical simulation and microstructural development in hardening cement-based materials”. In: *Heron* 37.3 (1992), pp. 1–61.

[84] F.-J. Ulm and O. Coussy. “Modeling of thermo-chemical-mechanical couplings of concrete at early age”. In: *Journal of Engineering Mechanics, ASCE* 121.7 (1995), pp. 785–794.

[85] F.-J. Ulm and O. Coussy. “Strength growth as chemo-plastic hardening in early age concrete”. In: *Journal of Engineering Mechanics, ASCE* 122.12 (1996), pp. 1123–1132.

[86] Z.P. Bažant and S. Prasannan. “Solidification theory for concrete creep. I: Formulation, II: verification and application.” In: *Journal of Engineering Mechanics* 115.7 (1989), pp. 1691–1725.

[87] J. Duchesne and M. A. Bérubé. “The effectiveness of supplementary cementing materials in suppressing expansion due to ASR: Another look at the reaction mechanisms part 1: Concrete expansion and portlandite depletion.” In: *Cement and Concrete Research* 21.1 (1994), pp. 73–82.

[88] B. Persson. “Seven-year study on the effect of silica fume in concrete.” In: *Advanced cement based materials* 7 (1998), pp. 139–155.

[89] D. R. G. Mitchell, I. Hinczak, and R. A. Day. “Interaction of silica fume with calcium hydroxide solutions and hydrated cement pastes.” In: *Cement and Concrete Research* 28.11 (1998), pp. 1571–1584.

[90] V. G. Papadakis. “Experimental investigation and theoretical modeling of silica fume activity in concrete.” In: *Cement and Concrete Research* 29 (1999), pp. 79–86.

[91] K. Takemoto and H. Uchikawa. “Hydration of pozzolanic cement”. In: *Proceedings of the 7th International Congress on Chemistry of Cement*. Paris, 1980, Vol. I, 1–29.

[92] S. Wild, B.B. Sabir, and J.M. Khatib. “Factors influencing strength development of concrete containing silica fume.” In: *Cement and Concrete Research* 25.7 (1995), pp. 1567–1580.

[93] J. Zelić, D. Rušić, D. Veža, and R. Krstulović. “The role of silica fume in the kinetics and mechanisms during the early stage of cement hydration.” In: *Cement and Concrete Research* 30 (2000), pp. 1655–1662.

[94] B. Persson. “Eight-year exploration of shrinkage in high-performance concrete.” In: *Cement and Concrete Research* 32 (2002), pp. 1229–1237.

[95] R.F. Feldman. "Sorption and length-change scanning isotherms of methanol and water on hydrated Portland cement." In: *Proceedings of the 5th International Congress on the Chemistry of Cement.* 1968, pp. 53–66.

[96] V. Baroghel-Bouny, M. Mainguy, T. Lassabatere, and O. Coussy. "Characterization and identification of equilibrium and transfer moisture properties for ordinary and high-performance cementitious materials." In: *Cement and Concrete Research* 29 (1999), pp. 1225–1238.

[97] Martin Z. Bažant and Zdenek P. Bažant. "Theory of sorption hysteresis in nanoporous solids: Part I. snap-through instabilities; Part II. molecular condensation". In: *Journal of the Mechanics and Physics of Solids* 60.9 (2012), pp. 1644–1675.

[98] E. Masoero, G. Cusatis, and G. Di Luzio. "C–S–H gel densification: the impact of the nanoscale on self desiccation and sorption isotherms". In: *Cement and Concrete Research* 109 (2018), pp. 103–119.

[99] Stéphane Poyet. "Experimental investigation of the effect of temperature on the first desorption isotherm of concrete". In: *Cement and Concrete Research* 39.11 (2009), pp. 1052–1059.

[100] Jean-François Daian. "Condensation and isothermal water transfer in cement mortar Part I—Pore size distribution, equilibrium water condensation and imbibition". In: *Transport in porous media* 3.6 (1988), pp. 563–589.

[101] Jürgen Hundt, Hans Kantelberg, and Peter Schimmelwitz. *Zur Wärme-und Feuchtigkeitsleitung in Beton.* Ernst, 1977.

[102] Y. Xi, Z.P. Bažant, and H.M. Jennings. "Moisture diffusion in cementitious materials – Moisture Capacity and diffusivity". In: *Advanced cement based materials* 1 (1994), pp. 258–266.

[103] J. Karger and D.M. Ruthven. *Diffusion in Zeolites and Other Microporous Solids.* New York: John Wiley & Sons, 1992.

[104] M. Jooss and H.W. Reinhardt. "Permeability and diffusivity of concrete as function of temperature". In: *Cement and Concrete Research* 32 (2002), pp. 1497–1504.

[105] Steven Bryant and Martin Blunt. "Prediction of relative permeability in simple porous media". In: *Phys. Rev. A* 46 (4 1992), pp. 2004–2011. DOI: `10.1103/PhysRevA.46.2004`. URL: `https://link.aps.org/doi/10.1103/PhysRevA.46.2004`.

[106] T.W. Patzek and D.B. Silin. "Shape Factor and Hydraulic Conductance in Noncircular Capillaries: I. One-Phase Creeping Flow". In: *Journal of Colloid and Interface Science* 236.2 (2001), pp. 295–304. ISSN: 0021-9797. DOI: https://doi.org/10.1006/jcis.2000.7413. URL: https://www.sciencedirect.com/science/article/pii/S0021979700974137.

[107] J. Hundt and H. Kantelberg. "Sorptionsuntersuchungen an zemestein, zementmörtel und beton (in German)". In: *Deutscher Ausschuss für Stahlbeton* 297 (1978), pp. 25–39.

[108] Ahmed Mohammed Soliman. "Early-age shrinkage of ultra high-performance concrete: mitigation and compensating mechanisms". PhD thesis. 2011.